Detachment of an adhered micropillar from a dissimilar substrate

S. N. Khaderi[1], N. A. Fleck[1], E. Arzt[2], R. M. McMeeking[234]

[1] *Engineering Department, University of Cambridge, Trumpington Street, Cambridge CB2 1PZ, UK*
[2] *INM-Leibniz Institute for New Materials and Saarland University Campus D2 2, 66123 Saarbruecken, Germany*
[3] *Departments of Materials and Mechanical Engineering, University of California, Santa Barbara, CA 93106, USA*
[4] *School of Engineering, University of Aberdeen, King's College, Aberdeen AB24 2UE, UK*

Abstract

The mechanics of detachment is analysed for $2D$ flat-bottomed planar pillars and $3D$ cylindrical pillars from a dissimilar elastic substrate. Application of an axial stress to the free end of the pillar results in a singularity in stress at the corner with the substrate. An eigenvalue analysis reveals that the stress field near the corner is dominated by two singular eigenfields having eigenvalues (λ_1, λ_2) with corresponding intensities (H_1, H_2). The asymptotic stress field σ_{ij} is of the form $\sigma_{ij} = H_1 r^{\lambda_1 - 1} f_{ij}(\lambda_1, \theta) + H_2 r^{\lambda_2 - 1} f_{ij}(\lambda_2, \theta)$, where f_{ij} describe the angular dependence θ of σ_{ij}, and r is the radial distance from the corner. The stress intensities (H_1, H_2) are calculated numerically, using a domain integral approach, as a function of the elastic mismatch between the pillar and substrate. The singular zone extends across approximately 10% of the pillar diameter (in $3D$) or pillar width (in $2D$).

Interfacial failure is predicted for an assumed crack emanating from the corner of pillar and substrate. For the case of an interfacial crack that resides within the domain of corner singularity, a boundary layer analysis is performed to calculate the dependence of the interfacial stress intensity factor K upon (H_1, H_2). When the crack extends beyond the domain of corner singularity, it is necessary to consider the full geometry in order to obtain K. A case study explores the sensitivity of the pull-off stress to the flaw size and to the degree of material mismatch. The study has implications for the optimum design of adhesive surface micropatterns, for bonding to either stiffer or more compliant substrates.

1. Introduction

[Figure 1 about here.]

The recent design and fabrication of bio-inspired adhesive surfaces follows a new paradigm for reversible adhesion (eg. Jeong et al., 2009; Gorb et al., 2007; Greiner et al., 2007; Kamperman et al., 2010). Observation of the adhesion organs exhibited by some creatures of the animal kingdom, for example the beetle and gecko, has shown hair-like compliant structures at the tip of their limbs that enable them to climb on vertical walls

and hang from ceilings. Adhesion is primarily due to van der Waals forces (Autumn et al., 2002) with a humidity-dependent contribution from capillary forces (Huber et al., 2005). This has led to the concept of "contact splitting" (Arzt et al., 2003), according to which adhesion is enhanced by the presence of small, discrete and compliant ('fibrillar') contact elements.

The surfaces of artificial, bio-inspired adhesive surfaces typically have a micropattern comprising an array of short cylindrical pillars made from a soft material such as PDMS or other polymers. The diameter of individual pillars ranges from sub-micron to sub-millimeter dimensions, with length-to-diameter aspect ratios typically between 1 and 10. These pillars have been fabricated with a variety of tip shapes (flat-bottomed (Greiner et al., 2007) or mushroom-shaped (Gorb et al., 2007; Greiner et al., 2007; Murphy et al., 2009)) and geometries (straight (Greiner et al., 2007) or slanted (Jeong et al., 2009)). An example of an array of flat-bottomed micropillars is shown in Fig. 1. Such adhesive pillars have also been made from shape memory polymers (Reddy et al., 2007) and from flexible nickel paddles coated with polymeric nanorods (Northen et al., 2008). A switchable adhesion has been achieved in such systems by controlling temperature (Reddy et al., 2007), magnetic field (Northen et al., 2008) or compressive preload (Paretkar et al., 2013). Especially the latter system is now on the verge of practical application in industrial robotic systems.

For the optimization of artificial fibrillar surfaces, a full understanding is required of the micromechanical detachment mechanisms and the influences of the geometrical and materials parameters involved. When collective mechanisms and backing layer effects are neglected, the problem can be reduced to the detachment of a single elastic pillar from an elastic substrate. Furthermore, mechanisms that involve the collective behavior of many pillars, or that are motivated by the behavior of the layer of material backing a pillar array, depend on the manner in which individual pillars detach from the elastic substrate. This involves a strong interplay between surface energy and elastic strain energy. The detailed push-on/pull-off behaviour is sensitive to the contact shape and to the elastic mismatch between pillar and substrate. Much progress has been made for a conforming contact, where the bottom of the pillar is spherical (or cylindrical) in shape. For example, the Johnson-Kendall-Roberts (JKR) theory (Johnson et al., 1971) considers the elastic-brittle limit such that the traction-separation law of the interface enters the analysis only via the work of separation G_c . In this limit, the process zone (over which the force-separation law is active) is much smaller than the contact size. The domain of validity of the elastic-brittle idealisation has been explored (Paretkar et al., 2013; Northen et al., 2008), and found to have widespread application. Much less is known about the detachment of a non-conforming pillar, such as a flat-bottomed cylinder from a flat substrate.

Arrays of cylindrical pillars have been fabricated from PDMS (eg. del Campo et al., 2007). The tip of such pillars can be flat or rounded with a prescribed radius at the corner, see Fig. 1. Adhesion studies have been performed by del Campo et al. (2007), using these arrays, to measure the pull-off stress against a

sapphire spherical substrate. They report that the pull-off strength for an array of pillars with rounded tip is only a fraction that of flat-tipped pillars. Note that the pull-off stress for the array of pillars is governed by the pull-off stress for an individual pillar and the rounded tip can be considered to be a crack-like flaw. Consequently, it is important to have an accurate estimate for the pull-off stress for an individual pillar as a function of the crack length, pillar geometry and elastic mismatch between the pillar and substrate. This is the subject of the paper.

The pillar substrate geometry analysed is shown in Fig. 2. For this geometry, detachment begins at the corner of the pillar and propagates inwards. The details are made complex by the presence of a corner singularity in the perfectly bonded state, with the level of singularity sensitive to the degree of elastic mismatch between pillar and substrate. Furthermore, the geometry shown in Fig. 2(a) is the fundamental shape for a fibril undecorated by a special tip shape such as a mushroom head or a flange, but perhaps having an edge radius of curvature arising as a natural outcome of fabrication (see Fig. 1(b)). Such an edge radius can be represented to first order as the crack depicted in Fig. 2(c) with the its length being equal to the edge radius. Detachment at the tip of the crack/edge radius, shown in Fig. 2(c), is controlled by stresses arising from the edge singularity in the problem of Fig. 2(a). Solution of the problem depicted in Fig. 12(a) is thus of primary importance in the characterization and understanding of the detachment of micro-pillars from an elastic substrate dissimilar or similar to the material from which the pillar is made.

[Figure 2 about here.]

The purpose of the present paper is thus to present a comprehensive mechanics analysis for the detachment of a 2D flat-bottomed rectangular pillar of width D, and of a flat-bottomed pillar in the form of a 3D circular cylindrical pillar of diameter D, from a possibly dissimilar substrate, see Fig. 2(a). We take the 2D pillar to be sufficiently thick in the z-direction of Fig. 2(a) (i.e. in the through thickness direction) that plane strain conditions apply. Application of a remote axial stress to the pillar leads to a singularity in the stress field at the interface corner. For both $2D$ and $3D$ geometries, the level and intensity of the corner singularity are determined by our analysis in terms of coordinates r and θ, see Fig. 2(b). Both the pillar and substrate comprise isotropic elastic solids, labelled $m = 1$ and $m = 2$, respectively (shown in Fig. 2 by the labelling #1 and #2). The materials have shear moduli (μ_1, μ_2) and Poisson's ratios (ν_1, ν_2). A reduction in the number of independent elastic constants is achieved by means of the two Dundurs' parameters

$$\alpha = \frac{\mu_1(\kappa_2 + 1) - \mu_2(\kappa_1 + 1)}{\mu_1(\kappa_2 + 1) + \mu_2(\kappa_1 + 1)}, \quad \beta = \frac{\mu_1(\kappa_2 - 1) - \mu_2(\kappa_1 - 1)}{\mu_1(\kappa_2 + 1) + \mu_2(\kappa_1 + 1)}, \tag{1}$$

where $\kappa_m = 3 - 4\nu_m$. For the practical range of elastic constants, we find that $-1 < \alpha < 1$ and $0 < \beta < \alpha/4$, as discussed by Hutchinson and Suo (1992).

It is envisaged that crack-like defects pre-exist at the corner of both pillars, and detachment occurs when the energy release rate attains the interfacial adhesion energy or toughness G_c. As noted above, the crack-like defect at the corner can represent an edge radius naturally present due to fabrication. An asymptotic analysis is thus given for an interfacial crack embedded within the singular zone at the corner, see Fig. 2(c). Interfacial detachment is also analysed for the case where the crack extends beyond the domain of the corner singularity, see Fig. 2(d). For completeness, results are also reported in an appendix for the detachment of a planar pillar subjected to an end moment.

1.1. Outline of paper

The focus is on the asymptotic response for a short corner crack embedded within the singular stress field at the interface corner, as shown in Fig. 2(a). First, we analyse the corner singularity and determine the level of singularity λ and its intensity H as a function of material mismatch, see Fig. 2(b); we denote this *problem A*.

Second, we place a short corner crack on the interface between pillar and substrate, with the crack length ℓ taken to be sufficiently short that the crack is fully embedded within the elastic stress field of the corner singularity, see Fig. 2(c). An asymptotic analysis is developed in order to give the coupling between the interfacial stress intensity factor for the crack K and the intensity of the corner singularity H. We label this *problem B*.

For completeness, the stress intensity factor is obtained numerically for a long interfacial crack emanating from the corner, as sketch in Fig. 2(d); we denote this *problem C*. When the crack is sufficiently short the solution converges to the asymptotic solution for the short crack, as obtained by combining the solutions to problems A and B.

2. Methodology

It is instructive to summarise the overall mathematical framework for the three problems in turn.

2.1. Problem A: the corner singularity

A singular asymptotic stress field exists at the corner of the perfectly bonded 2D (or 3D) pillar (absent the interfacial crack). This stress field can be written in terms of a polar co-ordinate system (r, θ), centred on the left-hand corner of the pillar/substrate, see Fig. 2(b). The stress σ_{ij} and displacement u_j fields in the vicinity of the corner can be written as a series expansion of eigenstates

$$\sigma_{ij} = \sum_{n=1}^{\infty} H_n r^{\lambda_n - 1} f_{ij}(\lambda_n, \theta), \tag{2}$$

and

$$u_j = \sum_{n=1}^{\infty} H_n r^{\lambda_n} g_j(\lambda_n, \theta). \tag{3}$$

Here, λ_n are the eigenvalues, each term is of intensity H_n, and f_{ij} and g_j are the eigenfunctions that capture the angular dependence θ of stress σ_{ij} and displacement u_i, respectively. An eigenvalue analysis is given in Appendix A in order to obtain λ_n, f_{ij} and g_j for any given (α, β). The analysis reveals that, for a given elastic mismatch, there are two leading terms[1] in the series expansions of (2) and (3). The eigenvalues (λ_1, λ_2) both lie within the interval [0.5, 1] and the corresponding stress intensities for the corner singularity are (H_1, H_2). For example, when λ_1 equals 0.5, the level of singularity is identical to that of a crack in a homogeneous solid.

The scalars (H_1, H_2) give the intensity of the corner singularity and scale linearly with the applied axial stress σ^∞, as shown in Fig. 2(a). The asymptotic normal component of the stress field along $\theta = 0$ is given by

$$\sigma_{\theta\theta} = H_1 r^{\lambda_1 - 1} + H_2 r^{\lambda_2 - 1}. \tag{4}$$

From dimensional considerations we can express H_n for $n = (1, 2)$ in terms of σ^∞, and the pillar dimension D, according to

$$H_n = \sigma^\infty D^{1-\lambda_n} a_n(\alpha, \beta), \tag{5}$$

where the coefficient $a_n(\alpha, \beta)$ is determined numerically in section 3. Note that the magnitude of a_n differs for the plane strain (2D) and axisymmetric (3D) cases.

[Figure 3 about here.]

The asymptotic $H-$field at the corner of a pillar-substrate interface plays a similar role to the K-field at a crack tip. A crack propagates in a brittle manner when the magnitude of the applied K-field reaches a critical value. Likewise, it has been envisaged by Akisanya and Fleck (1997) that the pillar-substrate interface can fail in a brittle manner when the value of the corner stress intensity H_1 reaches a critical value H_c. The value H_c can be can be measured by performing experiments for any combination of elastic mismatch.

2.2. Problem B: a short interfacial crack embedded within the corner singularity

Now consider an interfacial crack of length ℓ, see Fig. 2(c). The crack is an edge crack, in plane strain, for the 2D pillar, and is an external annular crack in the 3D case. When the crack is sufficiently short that it is embedded within the corner singularity, the complex stress intensity factor K for the interfacial crack

[1] This contrasts with the asymptotic stress field near a crack, where a single singular term exists near the crack tip.

can be expressed in terms of H_n. As a brief aside and in order to introduce notation, we recall the definition of K and of related fracture mechanics parameters for an interfacial crack.

Consider the asymptotic stress field in the vicinity of an interfacial crack in terms of the polar coordinates (R, Θ) centred on the crack tip, see Fig. 2(c). Directly ahead of the crack tip, the hoop stress $\sigma_{\Theta\Theta}$ and shear stress $\sigma_{R\Theta}$ read (Hutchinson and Suo, 1992)

$$\sigma_{\Theta\Theta} + i\sigma_{R\Theta} = \frac{K}{\sqrt{2\pi R}} R^{i\epsilon}, \tag{6}$$

where K is the complex stress intensity factor with real part K_1 and imaginary part K_2. The oscillatory index ϵ depends upon β via

$$\epsilon = \frac{1}{2\pi} \ln \frac{1-\beta}{1+\beta}. \tag{7}$$

The mode mix $\hat{\psi}$ is defined via

$$\tan \hat{\psi} = \frac{\mathrm{Im}(K\hat{\ell}^{i\epsilon})}{\mathrm{Re}(K\hat{\ell}^{i\epsilon})}, \tag{8}$$

where $\hat{\ell}$ is an arbitrary distance ahead of the crack tip[2]. Upon choosing $\hat{\ell} = \ell$, the mode mix ψ is given by

$$\tan \psi = \frac{\mathrm{Im}(K\ell^{i\epsilon})}{\mathrm{Re}(K\ell^{i\epsilon})}, \tag{9}$$

and consequently the value of $\hat{\psi}$ for any other choice of $\hat{\ell}$ is

$$\hat{\psi} = \psi - \epsilon \ln \left(\frac{\ell}{\hat{\ell}} \right). \tag{10}$$

Typically, the difference between $\hat{\psi}$ and ψ is very small since ϵ is small and there is a logarithmic dependence upon $\ell/\hat{\ell}$. The energy release rate G scales with the stress intensity factor K according to (Hutchinson and Suo, 1992)

$$G = \frac{1-\beta^2}{E^*} \left(K_1^2 + K_2^2 \right), \tag{11}$$

where

$$\frac{16}{E^*} = \frac{1+\kappa_1}{\mu_1} + \frac{1+\kappa_2}{\mu_2}. \tag{12}$$

Now back to the problem of a short corner crack. To extract the interfacial stress intensity factor K, it suffices to analyse the boundary layer problem as defined in Fig. 2(c). Assume that the crack length ℓ is much smaller than the radius to the outer boundary r_b and prescribe the displacement (3) on the outer boundary. From dimensional considerations K can be related to (H_1, H_2) according to

$$K\ell^{i\epsilon} = H_1 \ell^{\lambda_1 - 1/2} d_1 + H_2 \ell^{\lambda_2 - 1/2} d_2, \tag{13}$$

[2]For the case $\beta = 0$, we have $\epsilon = 0$ and the mode mix becomes independent of $\hat{\ell}$.

where the complex calibration factors $d_n(\alpha,\beta)$, have real and imaginary components $d_n^R(\alpha,\beta)$ and $d_n^I(\alpha,\beta)$, respectively, for each $n=(1,2)$. We shall determine d_n by evaluation of the complex stress intensity factor $K\ell^{i\epsilon}$ in a plane strain finite element (FE) scheme, as detailed below in section 3. We emphasise that K depends on the remote loading only via the loading parameters (H_1,H_2), and the calibration factors d_n depends only on the elastic mismatch. Note that the values of (d_1,d_2) are the same for both the 2D and 3D problems as the crack tip and corner singularity are both in a state of plane strain. Upon making use of (5) and (13), the stress intensity factor scales with the remote tensile stress σ^∞ according to

$$\frac{Kl^{i\epsilon}}{\sigma^\infty \ell^{1/2}} = \left(\frac{\ell}{D}\right)^{\lambda_1-1} a_1 d_1 + \left(\frac{\ell}{D}\right)^{\lambda_2-1} a_2 d_2. \tag{14}$$

This formula reveals explicitly the dependence of the K-calibration on the level of corner singularity λ_n, and on the product of the two calibration factors, $a_n d_n$.

2.3. Problem C: a long interfacial crack emanating from the corner

When the crack extends beyond the H-dominated zone, the stress intensity factor K is extracted by performing FE simulations using the full geometry as shown in Fig. 2(d). From dimensional considerations we have

$$K\ell^{i\epsilon} = \sigma^\infty \ell^{1/2} b, \tag{15}$$

where the complex calibration factor $b = b_R + ib_I$ depends on the elastic mismatch (α,β), on the geometry (ℓ/D) and whether the pillar is 2D or 3D. The function b is evaluated numerically as described in section 3. We anticipate that, in the limit of a short corner crack, as $\ell \to 0$, we have

$$b \to \left(\frac{\ell}{D}\right)^{\lambda_1-1} a_1 d_1 + \left(\frac{\ell}{D}\right)^{\lambda_2-1} a_2 d_2. \tag{16}$$

The energy release rate can be written in terms of b, via (15), as

$$G = \frac{1-\beta^2}{E^*}\left(K_1^2 + K_2^2\right) = \frac{1-\beta^2}{E^*}\left(\sigma^\infty\right)^2 \ell |b|^2, \tag{17}$$

and the phase angle ψ can be written as

$$\tan\psi = \frac{\mathrm{Im}(K\ell^{i\epsilon})}{\mathrm{Re}(K\ell^{i\epsilon})} = \frac{b_I}{b_R}. \tag{18}$$

3. Numerical analysis

3.1. Prediction of corner stress intensity factor H_n in Problem A

We adopt the method of Akisanya and Fleck (1997), in order to calculate the calibration factors (a_1,a_2) for (H_1,H_2), as defined in (5). The method is briefly outlined as follows. A finite element analysis of the

geometry shown in Fig. 2(b) is performed in order to determine the elastic field due to a remote tensile stress σ^{∞}. Write (σ_{ij}, u_j) as the actual stress and displacement field, and (σ^*_{ij}, u^*_j) as a suitably chosen auxiliary field. The field (σ^*_{ij}, u^*_j) associated with the choice of $\lambda^* = -\lambda$ is an acceptable eigenfield and satisfies the boundary conditions at the corner. Although this field is too singular to be physically valid, it provides a useful means of extracting the values of (H_1, H_2) in problem A. We first outline the procedure to calculate H_1.

The reciprocal theorem can be stated as

$$\oint_C \left(\sigma_{ij} u^*_i - \sigma^*_{ij} u_i\right) n_j dS = 0, \tag{19}$$

where n_j is the unit normal to the closed contour C, as shown in Fig. 4. We proceed to take the starred field in the above equation to be the eigenfield associated with $\lambda^* = -\lambda_1$. This auxiliary field is given by

$$\sigma^*_{ij} = H^* r^{\lambda^* - 1} f_{ij}(\lambda^*, \theta), \tag{20}$$

and

$$u^*_j = H^* r^{\lambda^*} g_j(\lambda^*, \theta). \tag{21}$$

It suffices to take $H^* \equiv 1$ for our purposes.

Now subdivide the contour into 4 constituents as shown in Fig. 4, labelled C_1 through C_4. The integrand of (19) vanishes on C_1 and C_3 since the eigenfields each satisfy the imposed boundary conditions. Consequently,

$$\int_{C_2} \left(\sigma_{ij} u^*_j - \sigma^*_{ij} u_i\right) n_j dS = -\int_{C_4} \left(\sigma_{ij} u^*_j - \sigma^*_{ij} u_i\right) n_j dS. \tag{22}$$

Now choose the contours C_2 and C_4 to have a radius of r_2 and r_4, respectively, as shown in Fig. 4. Both radii are taken to be sufficiently small that the local field (σ_{ij}, u_j) is adequately approximated by the sum of the first two terms of the asymptotic solution (2) and (3) for the corner singularity (with $n = 1$ and $n = 2$). We evaluate the line integral along C_2 by writing (σ_{ij}, u_j) and (σ^*_{ij}, u^*_j) in terms of (2) and (3), where H_1 and H_2 are unknown at this stage of calculation. We emphasise that this integral does not make use of the finite element solution for (σ_{ij}, u_j). In contrast, evaluation of the line integral along C_4 uses the finite element solution for (σ_{ij}, u_j) and the analytical auxiliary field (σ^*_{ij}, u^*_j). The value of H_1 and H_2 are extracted from (22), in the following manner.

First, consider the line integral over C_4. In order to improve numerical accuracy, following Li et al. (1985), we convert this line integral to a domain integral using the divergence theorem. Towards this end, introduce a linear function $q(r)$, such that it takes the value $q = 1$ on contour C_4 and $q = 0$ on the inner

contour C_2. Since the traction vanishes on the contours C_1 and C_3, we can write

$$-\int_{C_4}\left(\sigma_{ij}u_j^*-\sigma_{ij}^*u_i\right)n_j dS=-\int_C\left[q\left(\sigma_{ij}u_j^*-\sigma_{ij}^*u_i\right)\right]n_j dS. \tag{23}$$

Now use the divergence theorem on the right-hand side of (23) to obtain,

$$-\int_{C_4}\left(\sigma_{ij}u_j^*-\sigma_{ij}^*u_i\right)n_j dS=-\int_A\frac{\partial}{\partial x_j}\left[q\left(\sigma_{ij}u_j^*-\sigma_{ij}^*u_i\right)\right]dA, \tag{24}$$

where A is the area enclosed by C. Application of the reciprocal theorem and equilibrium equations provides the identity

$$-\int_A\frac{\partial}{\partial x_j}\left[q\left(\sigma_{ij}u_j^*-\sigma_{ij}^*u_i\right)\right]dA=-\int_A\left(\sigma_{ij}u_j^*-\sigma_{ij}^*u_i\right)\frac{\partial q}{\partial x_j}dA. \tag{25}$$

The area integral on the right hand side of (25) is evaluated numerically, using the values of (σ_{ij},u_j) from the FE simulations and the values of (σ_{ij}^*,u_j^*) from (20) and (21) . Thus we have solved for the integral over C_4 in (22).

Second, consider the line integral over the curve C_2 in (22). The elastic field (σ_{ij},u_j) is given by the eigenfield of (2) and (3), and the auxiliary field (σ_{ij}^*,u_j^*) is given by (20) and (21). Consequently, the line integral over contour C_2 can be written as

$$\begin{aligned}\int_{C_2}\left(\sigma_{ij}u_i^*-\sigma_{ij}^*u_i\right)n_j dS=H_1\int_{-\pi}^{\pi/2}&\left(f_{ij}(\lambda_1)g_i(-\lambda_1)-g_i(\lambda_1)f_{ij}(-\lambda_1)\right)n_j d\theta\\&+\frac{H_2}{r^{-\lambda_2+\lambda_1}}\int_{-\pi}^{\pi/2}\left(f_{ij}(\lambda_2)g_j(-\lambda_1)-g_j(\lambda_2)f_{ij}(-\lambda_1)\right)n_j d\theta.\end{aligned} \tag{26}$$

where f_{ij} and g_j are functions of θ. On noting that the above integral is independent of radius r of the contour, we have

$$\int_{C_2}\left(\sigma_{ij}u_i^*-\sigma_{ij}^*u_i\right)n_j dS=c_1H_1$$

where

$$c_1=\int_{-\pi}^{\pi/2}\left[f_{ij}(\lambda_1)g_i(-\lambda_1)-f_{ij}(-\lambda_1)g_i(\lambda_1)\right]n_j d\theta. \tag{27}$$

The value $c_1(\alpha,\beta)$ is calculated by numerical integration but is not reported here because it is only an intermediate result in the calculation of a_n. Upon equating (25) and (26) we evaluate the corner stress intensity H_1 as

$$H_1=-\frac{1}{c_1}\int_A\left(\sigma_{ij}u_j^*-\sigma_{ij}^*u_i\right)\frac{\partial q}{\partial x_j}dA.$$

A similar procedure can be invoked to extract H_2. Take the auxiliary eigenfield to have value $\lambda^*=-\lambda_2$ and take $H^*=1$, as before. Then

$$H_2=-\frac{1}{c_2}\int_A\left(\sigma_{ij}u_j^*-\sigma_{ij}^*u_i\right)\frac{\partial q}{\partial x_j}dA,$$

where c_2 is given by (27), upon replacing λ_1 with λ_2 and c_1 by c_2. From the calculated values of (H_1,H_2)

we deduce the values of the calibration coefficients (a_1, a_2) as defined in (5).

The FE simulation of the problem shown in Fig. 2(a) has been performed using ABAQUS commercial software[3]. The pillar has a length $L >> D$. For the 2D planar pillar, the substrate is taken to have a rectangular geometry of width $80D$ and thickness $40D$. For the 3D cylindrical pillar, the substrate is represented by a circular cylinder with a radius and thickness of $40D$. Numerical experimentation confirmed that these substrate dimensions are adequate to mimic a half-space. Only half of the geometry is modelled by symmetry. The displacement vanishes at the bottom of the substrate and a normal surface traction, of magnitude σ^{∞}, is applied to the free end of the pillar. The pillar and substrate are discretised using elements of type CPE8 in 2D and and CAX8 in 3D.

[Figure 4 about here.]

3.2. Prediction of interfacial stress intensity factor K for problems B and C

For the case of short cracks (i.e. Problem B), a crack of length ℓ is embedded in the H-dominated zone. The analysis is performed by prescribing a remote $H-$field over a boundary layer geometry, as shown in Fig. 2(c), and the challenge is to find the values of the complex calibration factors (d_1, d_2). Recall that the stress distribution in the $H-$dominated zone is identical for planar and cylindrical pillars, and the simulations are performed under plane strain conditions. To perform a boundary layer analysis, we choose a circular boundary layer of radius $r_b = 100l$ and centred on the left corner.

First, an asymptotic displacement field (3) of unit intensity $(H_1 = 1, H_2 = 0)$ is prescribed on the outer boundary. Again, the simulations are performed using ABAQUS software and displacement boundary conditions are imposed via a user subroutine. The stress intensity factors are extracted via the domain integral method within ABAQUS, and the calibration coefficient d_1 is determined using (13). Since the asymptotic stress field is identical for cylindrical and planar pillars (for a given elastic mismatch, crack length and H), the extracted values of $d(\alpha, \beta)$ are identical for planar and cylindrical pillars. Likewise, the values of the calibration coefficient d_2 are calculated by repeating the above procedure for $(H_1 = 0, H_2 = 1)$.

For long cracks (i.e. Problem C), the stress intensity factor cannot be extracted using a boundary layer geometry. In this case, an FE analysis is performed on the entire geometry as shown in 2(d) for both planar and cylindrical pillars. ABAQUS software is used to perform the analysis and obtain the stress intensity factors. From the extracted values of stress intensity factors, the complex calibration coefficients (b_1, b_2) are obtained via (15).

[3]Dassault Systems, Simulia Corporation, Providence, Rhode Island, USA. Version 6.11-1 is used to perform simulations.

4. Results

4.1. Problem A: corner singularity problem

4.1.1. Asymptotic stress field

As discussed in section 2, the asymptotic stress distribution is dominated by two eigenfields with eigenvalues λ_1 and λ_2. These are shown in Fig. 3(a). At $\alpha = -0.99$, the eigenvalues λ_1 and λ_2 are far apart ($\lambda_1 = 0.594$ and $\lambda_2 = 1$), and the asymptotic stress distribution is dominated by the singular field associated with λ_1. For $\alpha > -1$, both eigenvalues (λ_1, λ_2) are associated with singular fields and contribute towards the asymptotic solution. In the limit $\alpha \to 1$ and $\beta = 0$, the eigenvalues are $\lambda_1 = \lambda_2 = 0.5$ and give rise to crack singularities, see Fig 3(a). When $\beta = \alpha/4$, the eigenvalues (λ_1, λ_2) are real for $\alpha \leq 0.86$ and are complex for $\alpha > 0.86$, see Fig. 3(b). For the choice $\alpha = 1$ and arbitrary β, the complex eigenvalue λ is given by the formula $\lambda = 0.5 + i\epsilon$, as discussed in Appendix B. The results given in Fig. 3(b) for $\alpha = 1$ and $\beta = 0$, $\alpha/4$ support this.

In general, the asymptotic $H-$field gives rise to a shear traction on the interface in addition to the normal traction. The significance of the shear traction depends upon the degree to which the detachment mechanism is one of shear decohesion rather than normal decohesion. We proceed to evaluate the ratio χ_n of the shear traction to the normal traction for each eigenfield $n = 1$ and 2. Each eigenfield is normalised such that $f_{\theta\theta}(\lambda_n, \theta = 0) = 1$, and so $\chi_n = f_{r\theta}(\lambda_n, \theta = 0)$. It suffices to calculate $f_{r\theta}(\lambda_1, 0)$ and $f_{r\theta}(\lambda_2, 0)$ for various values of α and $\beta = 0, \alpha/4$. These results are plotted in Fig. 5 and given in table 1. There is significant shear component from each eigenfield to the interfacial traction, but the contributions are of opposite sign. Now, limit attention to $\beta = 0$ and evaluate $\sigma_{r\theta}/\sigma_{\theta\theta}$ for $\alpha \to -1$ and $\alpha \to 1$. For $\alpha \to -1$, we have $\lambda_1 = 0.594$ and $\lambda_2 = 1$. Then, as $r \to 0$ we have $\sigma_{r\theta}/\sigma_{\theta\theta} \approx f_{r\theta} = 0.5$. In contrast, for $\alpha \to 1$, we have $\lambda_1 = \lambda_2 = 0.5$. Then, $\sigma_{r\theta}/\sigma_{\theta\theta} = (a_1 - a_2) f_{r\theta}(\lambda_1, 0)/(a_1 + a_2)$. As a_1 approximately equals a_2 (see below) for $\alpha \to 1$ and $\beta = 0$, the shear stress on the interface vanishes.

[Figure 5 about here.]

4.1.2. The corner stress intensity H

We proceed to report the values of the calibration coefficients (a_1, a_2), as defined in (5), for a crack-free interface between a pillar (planar and cylindrical) and substrate. The calibration coefficients are calculated using the method outlined in section 3. The values of the calibration factors are obtained for $-1 < \alpha < 1$ and $\beta = 0$ and $\alpha/4$, and are plotted in Fig. 6. In general, the calibration factor a_1 decreases with increasing in α, and has only a mild dependence on β. In contrast, a_2 increases with increasing α and displays a maximum at $\alpha \approx 0.2$ for both $\beta = 0$ and $\beta = \alpha/4$. The same qualitative features arise for the dependence of (a_1, a_2) upon (α, β) for the cylindrical pillar. However, there is now a more marked sensitivity of a_2 upon

β. When λ is complex, (H_1, H_2) are replaced by a single complex value H, such that

$$\sigma_{\theta\theta} + i\sigma_{r\theta} = Hr^{\lambda-1}. \tag{28}$$

In the limit $\alpha \to 1$, an analytical formula exists for H, see (52) and (53) of Appendix B. The case of complex eigenvalues is discussed in more detail by Carpenter and Byers (1987), and is not discussed further here.

Now consider the limiting case where the pillar is compliant and the substrate is rigid, such that $\alpha = -1$. Akisanya and Fleck (1997) reported that a real singularity exists at the corner, such that

$$\sigma_{\theta\theta} = H_1 r^{\lambda_1 - 1} = \sigma^{\infty} \left(\frac{D}{r}\right)^{1-\lambda_1} a_1, \tag{29}$$

where $\lambda_1 = \lambda_1(\beta)$ and $a_1 = a_1(\beta)$. They found that the eigenvalue λ_1 increases from 0.59 to 0.69, and a_1 increases from 0.33 to 0.43 as β is varied from 0 to $\alpha/4$, in support of the results shown in Figs. 3 and 6 for $\alpha \to -1$.

[Figure 6 about here.]

[Table 1 about here.]

[Table 2 about here.]

It is instructive to compare the normal traction distribution of the full finite element solution with that of the asymptotic solution (involving the first two eigenvalues) in order to assess the domain of dominance of the two leading eigenfields, for selected (α, β). This comparison is shown in Fig. 7 (a),(b) for the planar pillar and in Fig. 7(c),(d) for the cylindrical pillar. It is clear from these results that the full FE solution converges to the asymptotic solution as $r/D \to 0$ in all cases considered. The convergence is similar for $\beta = 0$ in Figs. 7(a),(c) and $\beta = \alpha/4$ in Figs. 7(b),(d).

Define a cut-off length r_H as the distance from the corner at which the asymptotic solution is in error by 10%. We make use of plots such as those given in Fig. 7 in order to deduce r_H/D as a function of (α, β). The dependence of r_H/D upon α is given in Fig. 8 for $\beta = 0$, and a similar dependence exists for $\beta = \alpha/4$ (not shown). We conclude from Fig. 8 that the two leading terms of H-field suffice to describe the stress field near the corner up to a distance of $r_H/D \approx 0.1$ over the full range of α, for both pillars. The zone of H dominance is largest near $\alpha = 0$ for the cylindrical pillar, with a peak value of $r_H/D = 0.3$, see Fig. 8.

[Figure 7 about here.]

[Figure 8 about here.]

The calibration factors a_n for a 2D planar pillar subjected to a remote moment are reported in appendix C. It is instructive to compare the relative magnitudes of the calibration factors for bending with that for axial loading. The ratio of the calibration coefficients for the two problems is plotted as a function of α in Fig. 9(a) for $\beta = 0$ and in Fig. 9(b) for $\beta = \alpha/4$. The calibration factor for bending and for axial loading are denoted by $(a_n)_{bend}$ and $(a_n)_{axial}$, respectively. We note that $(a_1)_{bend}$ is less than $(a_1)_{axial}$ and their ratio is only mildly sensitive to the values of α and β. The ratio $(a_2)_{bend}/(a_2)_{axial}$ decreases with increasing α, and is only mildly sensitive to the magnitude of β.

[Figure 9 about here.]

4.2. Problem B: Stress intensity factor for short cracks

The stress intensity factor for a short crack embedded within an outer $H-$field is calculated using the boundary layer analysis, as discussed in section 3. Since the asymptotic H-field and crack tip fields are both plane strain, the calibration coefficients (d_1, d_2) are identical for the planar and cylindrical geometries. The calibration coefficients are plotted in Fig. 10(a) and (b) for $\beta = 0$ and $\beta = \alpha/4$, respectively. In broad terms the coefficients (d_1, d_2) have only a mild sensitivity to (α, β) except in the vicinity of $\alpha \to 1$.

[Figure 10 about here.]

4.3. Problem C: Stress intensity factor for long cracks

The stress intensity factor for a long crack is extracted by the domain integral method within ABAQUS. The calibration factor b is obtained as a function of ℓ/D for planar and cylindrical pillars via (15), and the values of b are given in Tables 3 and 4 for planar and cylindrical pillars, respectively, for selected values of α, with $\beta = 0$ and $\alpha/4$.

The normalised stress intensity factors $(Kl^{i\epsilon}/\sigma^\infty\sqrt{\ell})$ for planar and cylindrical pillars are shown in Figs. 11 and 12, respectively (labelled as 'long crack'). The asymptotic solution for the stress intensity factors (13) are included, and are labelled as 'short crack'. There is only a small effect of β value and geometry (planar versus cylindrical) upon the magnitude of $K\ell^{i\epsilon}$. The magnification in the value of $K\ell^{i\epsilon}/\sigma^\infty\sqrt{\ell}$ at small ℓ/D is due to the presence of the corner singularity. The role of α is mild, with $K\ell^{i\epsilon}$ increasing by a factor of about two as α increases from -1 to 1. For all material mismatches, the interfacial crack is close to mode I since $\mathrm{Im}(K\ell^{i\epsilon})$ is less than 1/2 that of $\mathrm{Re}(K\ell^{i\epsilon})$.

An analytical solution for b, in the limiting case of $\alpha = 1$ and any β, is given in appendix B, see (55). The imaginary part $\mathrm{Im}(K\ell^{i\epsilon})$ vanishes as $\alpha \to 1$ for $\beta = 0$, recall (54) and (58). The numerical solution for $(\alpha = 0.99, \beta = 0)$ is in excellent agreement with the analytical solution (55) for $(\alpha = 1, \beta = 0)$, and so there is no need to show the analytical case in Figs. 11 and 12 .

[Table 3 about here.]

[Table 4 about here.]

[Figure 11 about here.]

[Figure 12 about here.]

Denote by ℓ_s the crack length for which $K-$value, as calculated by the asymptotic analysis, differs from the full solution by 10%. Rephrased, ℓ_s is the maximum length of crack for which the short crack solution is valid. The value of ℓ_s is included in Fig. 8 for both plane strain and axisymmetric geometries with $\beta = 0$. For $-1 < \alpha < 0$, ℓ_s is almost insensitive to α, and the short crack solution is accurate for a crack shorter than $0.12D$ and $0.06D$ for planar and cylindrical pillars, respectively. For $0 < \alpha < 1$, ℓ_s decreases with increasing α. We note in passing that ℓ_s is somewhat less than r_H for the cylindrical pillar, but exceeds r_H for the planar pillar.

4.4. Energy release rate

The energy release rate G and phase angle ψ are extracted from K via (17) and (18), respectively, and are plotted as a function of ℓ/D in Fig. 13 for planar and cylindrical pillars, for $\alpha = \pm 0.99$ and $\alpha = 0$, with $\beta = 0$ and $\beta = \alpha/4$. Analytical solutions are included in the figure for α=1, as taken from (56) and (67). Excellent agreement is noted between the numerical prediction for $\alpha = 0.99$ and the analytical result for $\alpha = 1$. For the planar pillar, G increases by up to a factor of 2 as α is increased from -0.99 to 0.99. In contrast, G is only mildly sensitive to the magnitude of α for the cylindrical pillar. For both types of pillars, G increases with increasing ℓ/D, indicating that the interface will fail in an unstable manner for all combinations of (α, β) when a sufficient remote stress is applied. This is consistent with the simulations reported by Spuskanyuk et al. (2008).

Now consider the phase angle $\psi = \tan^{-1}[\mathrm{Im}(K\ell^{i\epsilon})/\mathrm{Re}(K\ell^{i\epsilon}])$. For both the 2D and 3D pillars, ψ is close to zero for $(\alpha = 0.99, \beta = 0)$ for all ℓ/D; this is anticipated since $(\alpha = 1, \beta = 0)$ corresponds to the case of a frictionless, rigid pillar (with zero shear traction on the interface). For any ℓ/D, ψ increases by up to 20° as α is decreased from +0.99 to -0.99, but ψ has only a mild sensitivity on the β-value.

[Figure 13 about here.]

5. Discussion

5.1. Case study

Recent studies of adhesion (Jeong et al., 2009; Gorb et al., 2007; Greiner et al., 2007; Kamperman et al., 2010) make use of PDMS pillars on a glass substrate[4] ($\alpha = -0.99, \beta = 0$) and of glass pillars on PDMS ($\alpha = 0.99, \beta = 0$). These pillars typically have rounded corners with a root radius r_c (see Fig. 1(b)). When such pillars are brought into contact with a substrate, the rounded corner between the pillar and substrate resembles a crack. The crack length can be taken as $\ell = r_c$. We can now make use of the above analysis in order to calculate the pull-off stress σ^∞ as a function of ℓ/D for both planar and cylindrical pillars. Upon equating the energy release rate in (17) to the interfacial adhesion energy or toughness G_c, we obtain (for $\beta = 0$)

$$\frac{\sigma^\infty D^{1/2}}{(E^* G_c)^{1/2}} = \left(\frac{D}{\ell} \frac{1}{(b_R^2 + b_I^2)} \right)^{1/2}. \tag{30}$$

This is plotted in Fig. 14. We note from Fig. 13 that ψ is in the range $0 \leq \psi \leq 20^\circ$ for both PDMS on glass and glass on PDMS, and so we can assume that G_c is close to its mode I value (pure tensile). Note that σ^∞ drops with increasing ℓ/D (implying an unstable response), and is mildly sensitive to the choice of materials for the pillar and substrate at short ℓ/D.

There is recent interest in the adhesion of PDMS pillars to human skin for the attachment of biomedical devices to skin (Kaiser et al., 2011). Here, we consider the detachment forces for a PDMS pillar from human skin. Skin has a shear modulus of approximately $\mu_2 = 0.1$ MPa and a Poisson's ratio ν_2=1/3 (Shergold et al., 2006). Then, the case of a PDMS pillar detaching from human skin corresponds to $\alpha \approx 0.8$ and $\beta \approx 0.2 = \alpha/4$. Upon equating the energy release rate in (17) to the interfacial adhesion energy or toughness G_c, we obtain (for $\beta = 0.2$)

$$\frac{\sigma^\infty D^{1/2}}{(E^* G_c)^{1/2}} = 1.02 \left(\frac{D}{\ell} \frac{1}{(b_R^2 + b_I^2)} \right)^{1/2}. \tag{31}$$

The normalised pull-off stress, calculated using (31), is shown in Fig. 14 as a function of ℓ/D. We note that the normalised pull-off stress for PDMS pillar from human skin is similar to that of a glass pillar from PDMS substrate.

[Figure 14 about here.]

[4] Assuming that the PDMS is compliant compared to glass and that the Young's modulus of PDMS E=2.6 MPa and Poisson's ratio ν=0.5 (Greiner et al., 2007).

5.2. Implications of the analysis

The above analysis assumes that the pillar detaches from the substrate in a brittle manner when the energy release rate (as determined from (11)) exceeds the interfacial adhesion energy or toughness G_c. Alternatively, the interface can fail in a 'ductile manner' when the normal stress at the interface reaches the cohesive strength σ_c. Whether the failure is ductile or brittle can be determined by comparing the size of the process zone at failure r_p to a characteristic size, which is the pillar diameter D in our case. If $r_p << D$, the pillar will detach in a brittle manner. The size of the process zone is given by $r_p = \Lambda E^* G_c/\sigma_c^2$, see Wang and Suo (1990). Here, Λ is a dimensionless parameter that depends on mode mix ψ and the elastic mismatch; it takes values ranging from 0.1 to 0.6. Assuming adhesion energy of $G_c = 50$ mJ/m^2 and a cohesive strength $\sigma_c = 0.1$ MPa for PDMS (Tang et al., 2005), r_p is in the range 1 μm to 5 μm. Hence, pillars of diameter $D > 5$ μm are likely to fail in a brittle manner and for such pillars the analysis given herein is applicable.

Figures 11 and 12 highlight the elevation in interfacial K for a crack embedded within the corner singularity. Consequently, the corner singularity reduces the detachment force for an adhered pillar. A mitigation strategy for this reduction in detachment force is to use a mushroom tip rather than a cylindrical tip, see for example Aksak et al. (2014) and Gorb et al. (2007). The mushroom tip reduces the magnitude of H, but no assessment of the reduction in H exists in the literature.

Figure 11 shows that the pull-off stress for the rigid pillar scales as $D^{-1/2}$, in agreement with the pull-off stress obtained by equating the Kendall equation (65) to the interfacial adhesion energy. Thus, small pillars will show higher pull-off stresses. Further, there is only a mild sensitivity to defect size. Our analysis also highlights the fact that a stiff pillar on a compliant substrate gives a smaller pull-off stress than a compliant pillar on a stiff substrate. However, the difference is less than a factor of 2 and may be masked by the presence of surface roughness or contaminant.

6. Concluding remarks

The present study highlights the role of the corner singularity in promoting the detachment of a micropillar from a substrate of dissimilar elastic properties. We assume that detachment occurs by the growth of an interfacial crack from the corner. A full asymptotic analysis has been performed for the stress intensity factor for an interfacial crack embedded within the corner singularity. On comparison with the full field solution, it is demonstrated that the two leading terms of the corner eigenfields contribute to the stress intensity factor of a short interfacial crack. The domain of singularity from the corner extends over a length of about 10% of the pillar diameter. As a consequence, the asymptotic analysis is of great utility as it a determination of the weakening effects of cracks present at the edge of the contact. In addition, the effect of a pillar edge radius on the detachment strength of the pillar under tension can be obtained by considering the edge radius to first

order to be a crack at the edge of the contact: the length of the crack is equal to the edge radius. Based on the interface adhesion energy, and the radius of the edge, we have derived an expression for the detachment strength of the pillar when subjected to tension. Therefore, our analysis has predictive power in regard to the tenacity of micropillars when one attempts to detach them from a substrate, whether that substrate is stiff or compliant relative to the pillar material. It remains to compare such a detachment strength with that of pillars having specialized tip shapes such as mushroom heads or flanges. An initial study along these lines has been performed recently by Aksak et al. (2014).

References

Akisanya, A., Fleck, N., 1997. Interfacial cracking from the freeedge of a long bi-material strip. International Journal of Solids and Structures 34 (13), 1645–1665.

Aksak, B., Sahin, K., Sitti, M., 2014. The optimal shape of elastomer mushroom-like fibers for high and robust adhesion. Beilstein Journal of Nanotechnology 5, 630–638.

Arzt, E., Gorb, S., Spolenak, R., 2003. From micro to nano contacts in biological attachment devices. Proceedings of the National Academy of Sciences 100 (19), 10603–10606.

Autumn, K., Sitti, M., Liang, Y. A., Peattie, A. M., Hansen, W. R., Sponberg, S., Kenny, T. W., Fearing, R., Israelachvili, J. N., Full, R. J., 2002. Evidence for van der waals adhesion in gecko setae. Proceedings of the National Academy of Sciences 99 (19), 12252–12256.

Carpenter, W. C., Byers, C., 1987. A path independent integral for computing stress intensities for v-notched cracks in a bi-material. International Journal of Fracture 35 (4), 245–268.

del Campo, A., Greiner, C., Arzt, E., 2007. Contact shape controls adhesion of bioinspired fibrillar surfaces. Langmuir 23 (20), 10235–10243.

Gao, H., Wang, X., Yao, H., Gorb, S., Arzt, E., 2005. Mechanics of hierarchical adhesion structures of geckos. Mechanics of Materials 37 (2), 275–285.

Gorb, S., Varenberg, M., Peressadko, A., Tuma, J., 2007. Biomimetic mushroom-shaped fibrillar adhesive microstructure. Journal of The Royal Society Interface 4 (13), 271–275.

Greiner, C., del Campo, A., Arzt, E., 2007. Adhesion of bioinspired micropatterned surfaces: effects of pillar radius, aspect ratio, and preload. Langmuir 23 (7), 3495–3502.

Huber, G., Mantz, H., Spolenak, R., Mecke, K., Jacobs, K., Gorb, S. N., Arzt, E., 2005. Evidence for capillarity contributions to gecko adhesion from single spatula nanomechanical measurements. Proceedings of the National Academy of Sciences of the United States of America 102 (45), 16293–16296.

Hutchinson, J., Suo, Z., 1992. Mixed mode cracking in layered materials. Advances in applied mechanics 29 (63), 191.

Jeong, H. E., Lee, J.-K., Kim, H. N., Moon, S. H., Suh, K. Y., 2009. A nontransferring dry adhesive with hierarchical polymer nanohairs. Proceedings of the National Academy of Sciences 106 (14), 5639–5644.

Johnson, K., 1987. Contact mechanics. Cambridge university press.

Johnson, K., Kendall, K., Roberts, A., 1971. Surface energy and the contact of elastic solids. Proceedings of the Royal Society of London. A. Mathematical and Physical Sciences 324 (1558), 301–313.

Kachanov, M. L., Shafiro, B., Tsukrov, I., 2003. Handbook of elasticity solutions. Springer.

Kaiser, J. S., Kamperman, M., de Souza, E. J., Schick, B., Arzt, E., 2011. Adhesion of biocompatible and biodegradable micropatterned surfaces. The International journal of artificial organs 34 (2), 180–184.

Kamperman, M., Kroner, E., del Campo, A., McMeeking, R. M., Arzt, E., 2010. Functional adhesive surfaces with gecko effect: the concept of contact splitting. Advanced Engineering Materials 12 (5), 335–348.

Kendall, K., 1971. The adhesion and surface energy of elastic solids. Journal of Physics D: Applied Physics 4 (8), 1186.

Li, F. Z., Shih, C. F., Needleman, A., 1985. A comparison of methods for calculating energy release rates. Engineering Fracture Mechanics 21 (2), 405–421.

Mossakovskii, V., 1963. Compression of elastic bodies under conditions of adhesion (axisymmetric case). Journal of Applied Mathematics and Mechanics 27 (3), 630–643.

Murphy, M. P., Aksak, B., Sitti, M., 2009. Gecko-inspired directional and controllable adhesion. Small 5 (2), 170–175.

Muskhelishvili, N., 1977. Some basic problems of the mathematical theory of elasticity. No. 1. Springer.

Northen, M. T., Greiner, C., Arzt, E., Turner, K. L., 2008. A gecko-inspired reversible adhesive. Advanced Materials 20 (20), 3905–3909.

Paretkar, D., Kamperman, M., Martina, D., Zhao, J., Creton, C., Lindner, A., Jagota, A., McMeeking, R., Arzt, E., 2013. Preload-responsive adhesion: effects of aspect ratio, tip shape and alignment. Journal of The Royal Society Interface 10 (83).

Reddy, S., Arzt, E., del Campo, A., 2007. Bioinspired surfaces with switchable adhesion. Advanced Materials 19 (22), 3833–3837.

Shergold, O. A., Fleck, N. A., Radford, D., 2006. The uniaxial stress versus strain response of pig skin and silicone rubber at low and high strain rates. International Journal of Impact Engineering 32 (9), 1384–1402.

Spuskanyuk, A., McMeeking, R., Deshpande, V., Arzt, E., 2008. The effect of shape on the adhesion of fibrillar surfaces. Acta Biomaterialia 4 (6), 1669–1676.

Tang, T., Hui, C.-Y., Glassmaker, N. J., 2005. Can a fibrillar interface be stronger and tougher than a non-fibrillar one? Journal of The Royal Society Interface 2 (5), 505–516.

Wang, J.-S., Suo, Z., 1990. Experimental determination of interfacial toughness curves using brazil-nut-sandwiches. Acta Metallurgica et Materialia 38 (7), 1279–1290.

Appendix A Asymptotic analysis of stress distribution near a corner

The asymptotic solution for the stress and displacement fields near a bi-material corner is derived below. Consider a bi-material corner as shown in Fig.2(b). Let (r,θ) be a cylindrical polar coordinate system originating at the corner. The material above and below the interface is numbered 1 and 2, respectively. Both materials 1 and 2 are isotropic, with shear moduli (μ_1,μ_2) and Poisson ratios (ν_1,ν_2). The elastic mismatch can be quantified using the Dundurs' parameters (α,β) as defined in (1). Introduce m as the index that identifies the material above ($m=1$) or below ($m=2$) the interface with $\kappa_m = 3-4\nu_m$. Following Muskhelishvili (1977), the stress and displacements in material 1 and 2 can be expressed in terms of complex potentials $\Phi_{(m)}(z)$ and $\Omega_{(m)}(z)$ as

$$\begin{aligned}
\sigma^{(m)}_{\theta\theta} - i\sigma^{(m)}_{r\theta} &= \bar{\Phi}'_{(m)}(\bar{z}) + \Phi'_{(m)}(z) + \bar{z}\bar{\Phi}''_{(m)}(\bar{z}) + z^{-1}\bar{z}\bar{\Omega}'_{(m)}(\bar{z}), && \text{(32a)}\\
\sigma^{(m)}_{rr} + i\sigma^{(m)}_{r\theta} &= \bar{\Phi}'_{(m)}(\bar{z}) + \Phi'_{(m)}(z) - \bar{z}\bar{\Phi}''_{(m)}(\bar{z}) - z^{-1}\bar{z}\bar{\Omega}'_{(m)}(\bar{z}), && \text{(32b)}\\
u^{(m)}_r + iu^{(m)}_\theta &= (2\mu_{(m)})^{-1}e^{-i\theta}\left(\kappa_{(m)}\Phi_{(m)}(z) - z\bar{\Phi}'_{(m)}(\bar{z}) - \bar{\Omega}_{(m)}(\bar{z})\right), && \text{(32c)}
\end{aligned}$$

where $z = x+iy = re^{i\theta}$, $(\,)'$ denotes the derivative and $\bar{(\,)}$ represents the complex conjugate, in the usual manner. Each complex potential can be written as a series expansion in z, where the origin is at the corner between pillar 1 and substrate 2. For example, we can write

$$\Phi_1(z) = \sum_{n=1}^{\infty} A_n z_n^{\lambda_n} \tag{33}$$

and likewise for Φ_2, Ω_1 and Ω_2. We make use of the traction boundary conditions on the pillar and substrate and continuity relations on the interface in order to derive a characteristic equation with roots λ_n. Now consider one such root and call it λ. We seek an asymptotic solution of the form

$$\begin{aligned}
\Phi_1 = Az^\lambda, \quad \Omega_1 = Bz^\lambda && \text{(34)}\\
\Phi_2 = Cz^\lambda, \quad \Omega_2 = Dz^\lambda, && \text{(35)}
\end{aligned}$$

where λ is the eigenvalue and the complex coefficients (A,B,C,D) form an associated eigenvector, to be determined. The relations (32a) and (32c) provide

$$\begin{aligned}
\sigma^{(1)}_{\theta\theta} + i\sigma^{(1)}_{r\theta} &= \lambda r^{\lambda-1}\left[Ae^{i(\lambda-1)\theta} + \lambda\bar{A}e^{-i(\lambda-1)\theta} + \bar{B}e^{-i(\lambda+1)\theta}\right] && \text{(36a)}\\
\sigma^{(2)}_{\theta\theta} + i\sigma^{(2)}_{r\theta} &= \lambda r^{\lambda-1}\left[Ce^{i(\lambda-1)\theta} + \lambda\bar{C}e^{-i(\lambda-1)\theta} + \bar{D}e^{-i(\lambda+1)\theta}\right] && \text{(36b)}\\
u^{(1)}_r + iu^{(1)}_\theta &= \tfrac{r^\lambda}{2\mu^1}\left[\kappa_1 Ae^{i(\lambda-1)\theta} - \bar{A}\lambda e^{-i(\lambda-1)\theta} - \bar{B}e^{-i(\lambda+1)\theta}\right] && \text{(36c)}\\
u^{(2)}_r + iu^{(2)}_\theta &= \tfrac{r^\lambda}{2\mu^2}\left[\kappa_2 Ce^{i(\lambda-1)\theta} - \bar{C}\lambda e^{-i(\lambda-1)\theta} - \bar{D}e^{-i(\lambda+1)\theta}\right]. && \text{(36d)}
\end{aligned}$$

The displacements and tractions are continuous on the interface, and the tractions vanish on $\theta=\pi/2$ and $\theta=-\pi$, hence

$$\begin{aligned}
A + \lambda\bar{A} + \bar{B} - C - \lambda\bar{C} - \bar{D} = 0, && \text{(37a)}\\
\kappa_1 A - \lambda\bar{A} - \bar{B} - \mu\left(\kappa_2 C - \lambda\bar{C} - \bar{D}\right) = 0, && \text{(37b)}\\
Ae^{i\pi\lambda} - \lambda\bar{A} + \bar{B} = 0, && \text{(37c)}\\
Ce^{-i2\pi\lambda} + \lambda\bar{C} + \bar{D} = 0, && \text{(37d)}
\end{aligned}$$

where $\mu = \mu_1/\mu_2$. Note that (37c) and (37d) give B and D in terms of A and C, as

$$\bar{B} = -\left(Ae^{i\pi\lambda} - \lambda\bar{A}\right) \tag{38a}$$

$$\bar{D} = -\left(Ce^{i2\pi\lambda} + \lambda\bar{C}\right), \tag{38b}$$

and consequently, (37a) and (37b) can be re-expressed as

$$A(1 - e^{i\pi\lambda}) + 2\bar{A}\lambda + C(e^{-2i\pi\lambda} - 1) = 0, \tag{39a}$$

$$-(\kappa_2 + e^{-2i\pi\lambda})C\mu + A(\kappa_1 + e^{i\pi\lambda}) - 2\bar{A}\lambda = 0. \tag{39b}$$

We write $A = A_R + iA_I$, and likewise for B, C and D. The real and imaginary parts of the above equations give

$$(\cos(2\,\pi\lambda) - 1)C_R + (2\,\lambda - \cos(\pi\lambda) + 1)A_R + A_I \sin(\pi\lambda) + C_I \sin(2\,\pi\lambda) = 0, \tag{40a}$$

$$(\cos(2\,\pi\lambda) - 1)C_I - (2\,\lambda + \cos(\pi\lambda) - 1)A_I - A_R \sin(\pi\lambda) - C_R \sin(2\,\pi\lambda) = 0, \tag{40b}$$

$$-(\kappa_2 + \cos(2\,\pi\lambda))C_R\mu - C_I\mu \sin(2\,\pi\lambda) + (\kappa_1 - 2\,\lambda + \cos(\pi\lambda))A_R - A_I \sin(\pi\lambda) = 0, \tag{40c}$$

$$-(\kappa_2 + \cos(2\,\pi\lambda))C_I\mu + C_R\mu \sin(2\,\pi\lambda) + (\kappa_1 + 2\,\lambda + \cos(\pi\lambda))A_I + A_R \sin(\pi\lambda) = 0. \tag{40d}$$

We proceed to solve for C_R and C_I using (40a) and (40b) to obtain

$$C_R = \frac{(2\,\lambda - 2\,\cos(\pi\lambda) + 1)\,A_R \sin(\pi\lambda) - ((2\,\lambda - 1)\cos(\pi\lambda) + \cos(2\pi\lambda))A_I}{2\,\sin(\pi\lambda)}, \tag{41a}$$

$$C_I = -\frac{(2\,\lambda + 2\,\cos(\pi\lambda) - 1)\,A_I \sin(\pi\lambda) + ((2\,\lambda + 1)\cos(\pi\lambda) - \cos(2\pi\lambda))\,A_R}{2\,\sin(\pi\lambda)}, \tag{41b}$$

and upon substituting for (C_R, C_I) into (40c), and (40d) and equating the determinant of the coefficient matrix for (A_R, A_I) to zero, we obtain the characteristic equation $F(\lambda) = 0$, where

$$\begin{aligned} F(\lambda) = \big\{ &\left[4\left(\kappa_1^2 - 4\,\lambda^2 + 1\right) + 8\kappa_1 \cos(\pi\lambda)\right] \sin^2 \pi\lambda \\ &- 2\left[\left(\cos\pi\lambda + 2\lambda^2 - 1\right)\left(4\kappa_2 \cos^2 \pi\lambda + (\kappa_2 - 1)^2\right)\right]\mu^2 \\ &-4\left((\kappa_2 - 1)\left[4\lambda^2 \sin^2 \pi\lambda - (\kappa_1 - 1)\cos^2 \pi\lambda\right] + (\kappa_1\kappa_2 + 1)(1 - \sin 2\pi\lambda \sin\pi\lambda) - (\kappa_1 + \kappa_2)\right)\mu\big\} \,/\, \left\{4\sin^2 \pi\lambda\right\}. \end{aligned} \tag{42}$$

Without loss of generality, choose $\mu_1 = 1$ and $\kappa_1 = 0$. Then, for a given combination of (α, β), we calculate the values of μ_2 and κ_2. Any root of $F(\lambda) = 0$, which delivers a value of λ in the range $0 < \lambda < 1$, gives rise to an unbounded stress as $r \to 0$, and thence to a singular stress field. It is noted that for, $\alpha = -1$, there is only one root that results in a singular stress field. For larger α, there are two roots that result in singular stress field. The characteristic equation $F(\lambda) = 0$ is solved numerically for these two roots for various choices of (α, β). These are labelled (λ_1, λ_2), with $\lambda_1 < \lambda_2$. As discussed in section 2, we limit our attention to $-1 \le \alpha \le -1$ and $\beta = 0$ and $\alpha/4$.

The eigenvalues are shown in Fig. 3(a). When $\beta = 0$, a real root for λ exists for all values for α. When $\beta = \alpha/4$, the root λ becomes complex for $\alpha > 0.86$. The real and imaginary values of λ are given in Fig. 3(b) for $\alpha > 0.86$ and $\beta = \alpha/4$. We note in passing that (i) if λ is a solution to the characteristic equation, then $-\lambda$ is also a solution and (ii) the calculated values of λ for the limiting case of $\alpha \to -1$ are in good agreement with those reported by Akisanya and Fleck (1997).

For each eigenvalue λ, there exists an eigenfield with non-trivial solution for the coefficients A, B, C and D. Using the boundary conditions (37a) - (37d), we can solve for these coefficients in terms of any one of the unknown coefficients, say A_R. It remains to express A_R in terms of the stress intensity H. Recall from (4) that each value of H_n is associated with an eigenvalue λ_n. We continue to consider one representative eigenvalue λ and the corresponding intensity H. In order to obtain the required relation between A_R and H, write the traction $\sigma_{\theta\theta}(\theta = 0)$ as

$$\sigma_{\theta\theta} = \mathrm{Re}\left(\lambda r^{\lambda-1}(A + \lambda\bar{A} + \bar{B})\right) \equiv H r^{\lambda-1}. \tag{43}$$

To proceed, we need the expressions for $\bar{B}$ and A_I in terms of A_R. Upon substituting for B, C and D from (38a), (41a) and (38b) into (37a), we obtain

$$A_I = \frac{(2\,(\kappa_2 - 1)\lambda - 2\,\kappa_2 \cos(\pi\lambda) + \kappa_2 - 1)\mu \sin(\pi\lambda) - 2\,(\kappa_1 - 2\,\lambda + \cos(\pi\lambda))\sin(\pi\lambda)}{\left(2\,\kappa_2 \cos(\pi\lambda)^2 + (2\,(\kappa_2 + 1)\lambda - \kappa_2 - 1)\cos(\pi\lambda) - \kappa_2 + 1\right)\mu + 2\,\cos(\pi\lambda)^2 - 2} A_R. \tag{44}$$

Now make use of (38a) to express $\bar{B}$ in terms of A_R and A_I, and thereby re-write (43) as $A_R \equiv y_1 H$, where

$$y_1 = -\frac{\left(2\,\kappa_2\cos(\pi\lambda)^2 + (2\,(\kappa_2+1)\lambda - \kappa_2 - 1)\cos(\pi\lambda) - \kappa_2 + 1\right)\mu + 2\,\cos(\pi\lambda)^2 - 2}{2\left((\kappa_1+1)\lambda\sin(\pi\lambda)^2 + \left((\kappa_2+1)\lambda\sin(\pi\lambda)^2 - (\kappa_2+1)\lambda - (2\,(\kappa_2+1)\lambda^3 - (\kappa_2+1)\lambda)\cos(\pi\lambda)\right)\mu\right)}.$$

Likewise, (44) can be written as $A_I \equiv y_2 H$, where

$$y_2 = -\frac{(2\,(\kappa_2-1)\lambda - 2\,\kappa_2\cos(\pi\lambda) + \kappa_2 - 1)\mu\sin(\pi\lambda) - 2\,(\kappa_1 - 2\,\lambda + \cos(\pi\lambda))\sin(\pi\lambda)}{2\left((\kappa_1+1)\lambda\sin(\pi\lambda)^2 + \left((\kappa_2+1)\lambda\sin(\pi\lambda)^2 - (\kappa_2+1)\lambda - (2\,(\kappa_2+1)\lambda^3 - (\kappa_2+1)\lambda)\cos(\pi\lambda)\right)\mu\right)}.$$

It remains to obtain (B, C, D) as a function of H via (38a), (38b) and (41a), to give

$$\left[\begin{array}{cccccccc} A_R & A_I & B_R & B_I & C_R & C_I & D_R & D_I \end{array}\right]^T = \left[\begin{array}{c} \mathbf{X}_1 \\ \mathbf{X}_2 \end{array}\right]\mathbf{Y}H \tag{45}$$

where

$$\boldsymbol{X}_1 = \left[\begin{array}{cc} 1 & 0 \\ 0 & 1 \\ x_{31} & x_{32} \\ x_{41} & x_{42} \end{array}\right];\quad \boldsymbol{X}_2 = \left[\begin{array}{cc} x_{51} & x_{52} \\ x_{61} & x_{62} \\ x_{71} & x_{72} \\ x_{81} & x_{82} \end{array}\right]\boldsymbol{Y} = \left[\begin{array}{c} y_1 \\ y_2 \end{array}\right]; \tag{46}$$

with

$$x_{31} = (\lambda - \cos(\pi\lambda)) \tag{47a}$$
$$x_{32} = (\sin(\pi\lambda)) \tag{47b}$$
$$x_{41} = (\sin(\pi\lambda)) \tag{47c}$$
$$x_{42} = (\lambda + \cos(\pi\lambda)) \tag{47d}$$
$$x_{51} = \lambda - \cos(\pi\lambda) + \frac{1}{2} \tag{47e}$$
$$x_{52} = -\frac{(2\,\lambda - 1)\cos(\pi\lambda) - 2\,\sin(\pi\lambda)^2 + 1}{2\,\sin(\pi\lambda)} \tag{47f}$$
$$x_{61} = -\frac{(2\,\lambda + 1)\cos(\pi\lambda) - 2\,\cos(\pi\lambda)^2 + 1}{2\,\sin(\pi\lambda)} \tag{47g}$$
$$x_{62} = -\lambda - \cos(\pi\lambda) + \frac{1}{2} \tag{47h}$$
$$x_{71} = -\lambda^2 + \lambda\cos(\pi\lambda) + \frac{1}{2}\,\lambda + \frac{1}{2} \tag{47i}$$
$$x_{72} = \frac{2\,\lambda\cos(\pi\lambda)^2 + \left(2\,\lambda^2 + \lambda - 1\right)\cos(\pi\lambda) - \lambda + 1}{2\,\sin(\pi\lambda)} \tag{47j}$$
$$x_{81} = -\frac{2\,\lambda\cos(\pi\lambda)^2 - \left(2\,\lambda^2 - \lambda - 1\right)\cos(\pi\lambda) - \lambda - 1}{2\,\sin(\pi\lambda)} \tag{47k}$$
$$x_{82} = \lambda^2 + \lambda\cos(\pi\lambda) + \frac{1}{2}\,\lambda - \frac{1}{2} \tag{47l}$$

The stresses $\sigma_{ij}^{(m)}$ and displacements $u_i^{(m)}$ are given by (36), with (A, B, C, D) expressed in terms of H via (45). Thus (36) can be re-expressed as

$$\sigma_{ij}^{(m)} = Hr^{\lambda-1}f_{ij}^{(m)}, \tag{48a}$$
$$u_i^{(m)} = Hr^{\lambda}g_i^{(m)}, \tag{48b}$$

where the functions $f_{ij}^{(m)}$ and $g_i^{(m)}$ are defined by

$$[g_r^{(m)}\ g_\theta^{(m)}\ f_{rr}^{(m)}\ f_{\theta\theta}^{(m)}\ f_{r\theta}^{(m)}]^T = \boldsymbol{N}_{(m)}\boldsymbol{X}_{(m)}\boldsymbol{Y}, \tag{49}$$

where

$$\boldsymbol{N}_{(m)} = \begin{pmatrix} \frac{\left(\kappa_{(m)}-\lambda\right)\cos((\lambda-1)\theta)}{2\mu_{(m)}} & \frac{\left(-\kappa_{(m)}+\lambda\right)\sin((\lambda-1)\theta)}{2\mu_{(m)}} & -\frac{\cos((\lambda+1)\theta)}{2\mu_{(m)}} & \frac{\sin((\lambda+1)\theta)}{2\mu_{(m)}} \\ \frac{\left(\kappa_{(m)}+\lambda\right)\sin((\lambda-1)\theta)}{2\mu_{(m)}} & \frac{\left(\kappa_{(m)}+\lambda\right)\cos((\lambda-1)\theta)}{2\mu_{(m)}} & \frac{\sin((\lambda+1)\theta)}{2\mu_{(m)}} & \frac{\cos((\lambda+1)\theta)}{2\mu_{(m)}} \\ -\left(\lambda^2-3\,\lambda\right)\cos\left((\lambda-1)\theta\right) & \left(\lambda^2-3\,\lambda\right)\sin\left((\lambda-1)\theta\right) & -\lambda\cos\left((\lambda+1)\theta\right) & \lambda\sin\left((\lambda+1)\theta\right) \\ \left(\lambda^2+\lambda\right)\cos\left((\lambda-1)\theta\right) & -\left(\lambda^2+\lambda\right)\sin\left((\lambda-1)\theta\right) & \lambda\cos\left((\lambda+1)\theta\right) & -\lambda\sin\left((\lambda+1)\theta\right) \\ \left(\lambda^2-\lambda\right)\sin\left((\lambda-1)\theta\right) & \left(\lambda^2-\lambda\right)\cos\left((\lambda-1)\theta\right) & \lambda\sin\left((\lambda+1)\theta\right) & \lambda\cos\left((\lambda+1)\theta\right) \end{pmatrix}. \quad (50)$$

Appendix B Analytical results for $\alpha = 1$

We summarise here analytical results taken from the literature for a rigid pillar adhered to an elastic substrate $\alpha = 1$, first for the planar pillar and second for the axisymmetric pillar.

B.1 Rigid planar pillar on elastic substrate

First analyse the case of an ideal contact in the *absence* of a corner crack, $\ell = 0$, as shown in Fig. 2(a). The problem is identical to the indentation of a half-space by a sticking punch of width D. The eigenfield at the interface corner is identical to that of an interfacial crack, and the traction on the interface reads

$$\sigma_{\theta\theta} + i\sigma_{r\theta} = \frac{Kr^{i\epsilon}}{\sqrt{2\pi r}} = Hr^{\lambda-1}. \quad (51)$$

An explicit formula for K can be obtained from literature (Johnson, 1987; Muskhelishvili, 1977) as,

$$K = \frac{1+\kappa_2}{\sqrt{2\pi\kappa_2}}\sigma^\infty D^{1/2-i\epsilon}. \quad (52)$$

Upon equating the terms in (51) we obtain

$$H = \frac{K}{\sqrt{2\pi}} \quad \text{and} \quad \lambda = \frac{1}{2} + i\epsilon. \quad (53)$$

Since the stress field at the corner (51) is that of an interfacial crack, we can ask what is the phase angle of this interfacial crack tip field? In view of the fact that the only length scale that enters (52) is D, we define a phase angle $\hat{\psi}$, based on the choice $\hat{\ell} = D$ in (8). We obtain directly from (52) the result $\hat{\psi} = 0$ for all β.

Consider now the case where an interfacial *corner crack is present* beneath the sticking punch (ℓ/D and β arbitrary). Since the pillar is rigid, the portion of the pillar not in contact with the substrate plays no role, and the above solution (52) applies, provided D is replaced by $D - 2\ell$ and σ^∞ is replaced by $\sigma^\infty D/(D-2\ell)$, to give

$$K = K_1 + iK_2 = \frac{(1+\kappa_2)}{\sqrt{2\pi\kappa_2}}\sigma^\infty \left(\frac{D}{\ell}\right)\left(\frac{D}{\ell}-2\right)^{\frac{1}{2}-i\epsilon}\ell^{\frac{1}{2}-i\epsilon}. \quad (54)$$

By equating (54) and (15), the calibration coefficient b is

$$b = \frac{(1+\kappa_2)}{\sqrt{2\pi\kappa_2}}\left(\frac{D}{l}\right)\left(\frac{D}{l}-2\right)^{-\frac{1}{2}-i\epsilon}, \quad (55)$$

the energy release rate G follows as

$$\frac{GE^*}{(\sigma^\infty)^2 l} = \frac{4}{\pi}\left[\frac{2l}{D}\left(1-\frac{2l}{D}\right)\right]^{-1}, \quad (56)$$

and the phase angle ψ, now based on ℓ, reads

$$\psi = \tan^{-1}\left(\frac{b_I}{b_R}\right) = -\epsilon\ln\left(\frac{D}{l}-2\right). \quad (57)$$

Note that the energy release rate G is independent of β, whereas the phase angle ψ depends upon β, and vanishes when $\beta = 0$.

B.2 Rigid cylindrical pillar on an elastic substrate

First analyse the case of an ideal contact in the absence of an circumferential interface crack, $\ell = 0$, as shown in Fig. 2(a). An analytic solution for the normal and shear stress on the interface is available only in quadrature form as follows. Introduce $\rho = 0.5 - r/D$, such that ρD is the distance from the centre-line of the pillar to the point of interest on the interface (at a distance r from the corner). Then, Mossakovskii (Mossakovskii, 1963; Kachanov et al., 2003) has derived the result

$$\frac{\sigma_{\theta\theta} + i\sigma_{r\theta}}{\sigma^\infty} = \frac{\epsilon(1-2\nu_2)}{\sqrt{\kappa_2}\,\ln\kappa_s\,\tanh(\pi\epsilon)}\frac{2}{\rho}\int_0^\rho \left(\frac{\rho\cos(\xi) + ix\sin(\xi)}{(\rho^2-x^2)^{1/2}(D^2-4x^2)}\right)dx, \tag{58}$$

where $\xi = -\epsilon\ln[(D+2x)/(D-2x)]$. The corner singularity has the same asymptotic nature as that of the sticking planar punch, which we know from (52) to be an interfacial crack tip field. It remains to obtain the magnitude and phase of K for the cylindrical case. Mossakovskii (1963) has given a closed form expression for the compliance $\mathcal{C}$ of a rigid pillar on a half-space,

$$\mathcal{C} = \frac{(1-2\nu_2)}{2D\mu_2\ln\kappa_2}. \tag{59}$$

The load on the pillar is $P = \pi\sigma^\infty D^2/4$, and the energy release rate G is

$$G = \frac{1}{2}\frac{P^2}{\pi D}\frac{\partial\mathcal{C}}{\partial(D/2)} = \frac{\pi}{16}\frac{(1-2\nu_2)}{\mu_2\ln\kappa_2}(\sigma^\infty)^2 D. \tag{60}$$

Recall that $|K|^2 = E^*G/(1-\beta^2)$, where $E^* = 4\mu_2/(1-\nu_2)$ from (12). Hence

$$|K|^2 = \frac{\pi}{8}\frac{(1-2\nu_2)}{(1-\nu_2)(1-\beta^2)\ln\kappa_2}(\sigma^\infty)^2 D. \tag{61}$$

Thus, we know directly $|K|$ but not its phase angle. We shall make use of (58) in order to obtain the phase angle as follows. The asymptotic stress field at the corner is of the form

$$\sigma_{\theta\theta} + i\sigma_{r\theta} = \frac{KD^{i\epsilon}}{\sqrt{2\pi r}}\left(\frac{r}{D}\right)^{i\epsilon}, \tag{62}$$

as $r \to 0$, following (6). Hence,

$$KD^{i\epsilon} = \lim_{r\to 0}(\sigma_{\theta\theta} + i\sigma_{r\theta})\left(\frac{r}{D}\right)^{-i\epsilon}\sqrt{2\pi r}. \tag{63}$$

We proceed to substitute (58) into (63) in order to evaluate $KD^{i\epsilon}$ numerically[5]. Note that $KD^{i\epsilon} = |K|e^{i\hat{\psi}}$, where $\hat{\psi}$ is given by (8) with $\hat{\ell} = D$. A fitting exercise gives

$$\hat{\psi} = -\frac{\ln 4}{2\pi}\ln(3-4\nu_2), \tag{64}$$

and is accurate to within 5%. Numerical evaluation of (63) confirms the validity of $|K|$ as given by (61).

Previously, the energy release rate and phase angle for a $3D$ cylindrical pillar has been estimated by Kendall (1971) and by Gao et al. (2005) by making use of the frictionless punch solution. For the case of a flat-bottomed circular cylindrical punch, without friction, the energy release rate is

$$G = \frac{\pi}{16}\frac{(1-\nu_2^2)}{E_2}D(\sigma^\infty)^2, \tag{65}$$

and this corner singularity is identical to that of a mode I crack, with stress intensity factor $K = \sigma^\infty(\pi D/8)^{1/2}$. The expression (65) for G is very close to that for the adhered pillar for $\alpha = 1$ and arbitrary β (that is, arbitrary ν_2). For example, the expression (65) is identical to that of (60) for $\nu_2 = 1/2$ (ie. $\beta = 0$), and deviates by only 9% when $\nu_2 = 0$. The mode mixes are also very similar. For the adhered pillar, $\hat{\psi}$, as defined by $\arg(KD^{i\epsilon})$, is given by $-\ln(3-4\nu_2)\ln 4/2\pi$. Thus, $\hat{\psi} = 0$ for $\nu_2 = 1/2$ and $\hat{\psi} = -13.8^\circ$ for $\nu_2 = 0$. In comparison, the frictionless punch generates a mode I $K-$field in substrate 2 for all ν_2.

In similar manner, the indentation solution for a frictionless planar punch (of width D) is very close to that of the $2D$ planar pillar for $\alpha = 1$, arbitrary β. The energy release rate at the corner singularity of a frictionless punch

[5]The quadrature in (63) is evaluated in Matlab for small but finite r, for any given β.

is identical to that for the adhered $2D$ pillar, for $\alpha = 1$ and arbitrary β,

$$G = \frac{1}{\pi}\frac{(1-\nu_2^2)}{E_2} D(\sigma^\infty)^2. \tag{66}$$

The frictionless punch generates a mode I crack tip field whilst the sticking pillar has $\hat{\psi}$ (based on D) equal to zero, recall (52).

It is useful to collect the above analytical results for compliance, energy release rate and phase angle for a frictionless and sticking punch, see table 5. We emphasise that the case of rigid pillar on an elastic substrate ($\alpha = 1$, arbitrary β) is identical to the case of rigid, sticking punch.

[Table 5 about here.]

Now consider the cylindrical pillar in contact with a substrate with a circumferential interface crack of length ℓ. Following the same arguments as for the planar pillar, we replace D with $D - 2\ell$ and σ^∞ with $\sigma^\infty D^2/(D-2\ell)^2$ in the expression (58) for the interfacial traction, (60) for G, and (61) for $|K|$. Thus, the expression for G now reads

$$G = \frac{\pi}{16}\frac{(1-2\nu_2)}{\mu_2 \ln\kappa_2}\frac{(\sigma^\infty)^2 D}{(1-2\ell/D)^3}. \tag{67}$$

The phase angle ψ, as defined in (9), is related to $\hat{\psi}$ of (64) according to (10), to give

$$\psi = -\epsilon \ln\left(\frac{D}{4l} - \frac{1}{2}\right). \tag{68}$$

Appendix C Pillar subjected to an end moment M

For completeness, we report the calibration factors for a planar pillar subjected to an end moment M (see Fig.15(a)). We again consider the three problems discussed in section 2. For the crack-free configuration the asymptotic stress field at the corner is of the same form as that of axial loading, and is given by (2). Hence, $\lambda(\alpha,\beta)$ and $d(\alpha,\beta)$ are the same as before. The definitions (5) and (15) still apply, with $\sigma^\infty = 6M/D^2$ redefined as the maximum bending stress at the outer fibre of the planer pillar. However, the calibration functions a and b change.

Problem A. The values of the calibration factor a for various values of (α,β) are obtained using finite element (FE) analysis, as described in section 3. The FE simulations are performed by choosing the length of the pillar to be $40D$ and by modelling the substrate as a rectangular domain of height and half width equal to $40D$. The end moment M is applied to the top of the pillar, via a linear distribution of normal traction. Since the applied moment is antisymmetric about the neutral plane, only the right half of the geometry is modelled. The geometry is discretised using plane strain finite elements (CPE8 in ABAQUS terminology). The calculated values of a are reported in table 6.

[Table 6 about here.]

Problem C. When the crack is long, the values of the stress intensity factor K have to be extracted by performing finite element analysis on the entire geometry as shown in Fig.15(b). The finite element analysis is performed as detailed above, and the stress intensity factors are calculated using the domain integral method in ABAQUS. From the extracted stress intensity factors, the values of the complex calibration coefficient b are calculated for selected values of of (α,β); these are listed in table 7.

[Table 7 about here.]

[Figure 15 about here.]

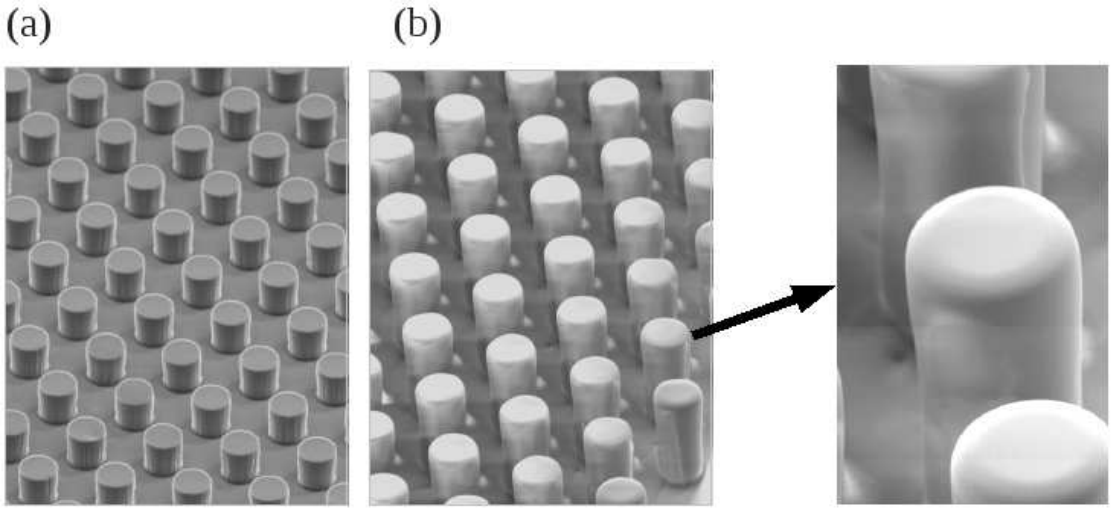

Figure 1: Arrays of flat-bottomed micropillars with (a) sharp and (b) rounded edges. Pillars have a radius of 10 μm and were fabricated out of polydimethylsiloxane (PDMS). Such 'artificial gecko structures' were found to have adhesion properties superior to unpatterned materials. Scanning electron micrographs adapted from del Campo et al. (2007) and Kaiser et al. (unpublished 2014).

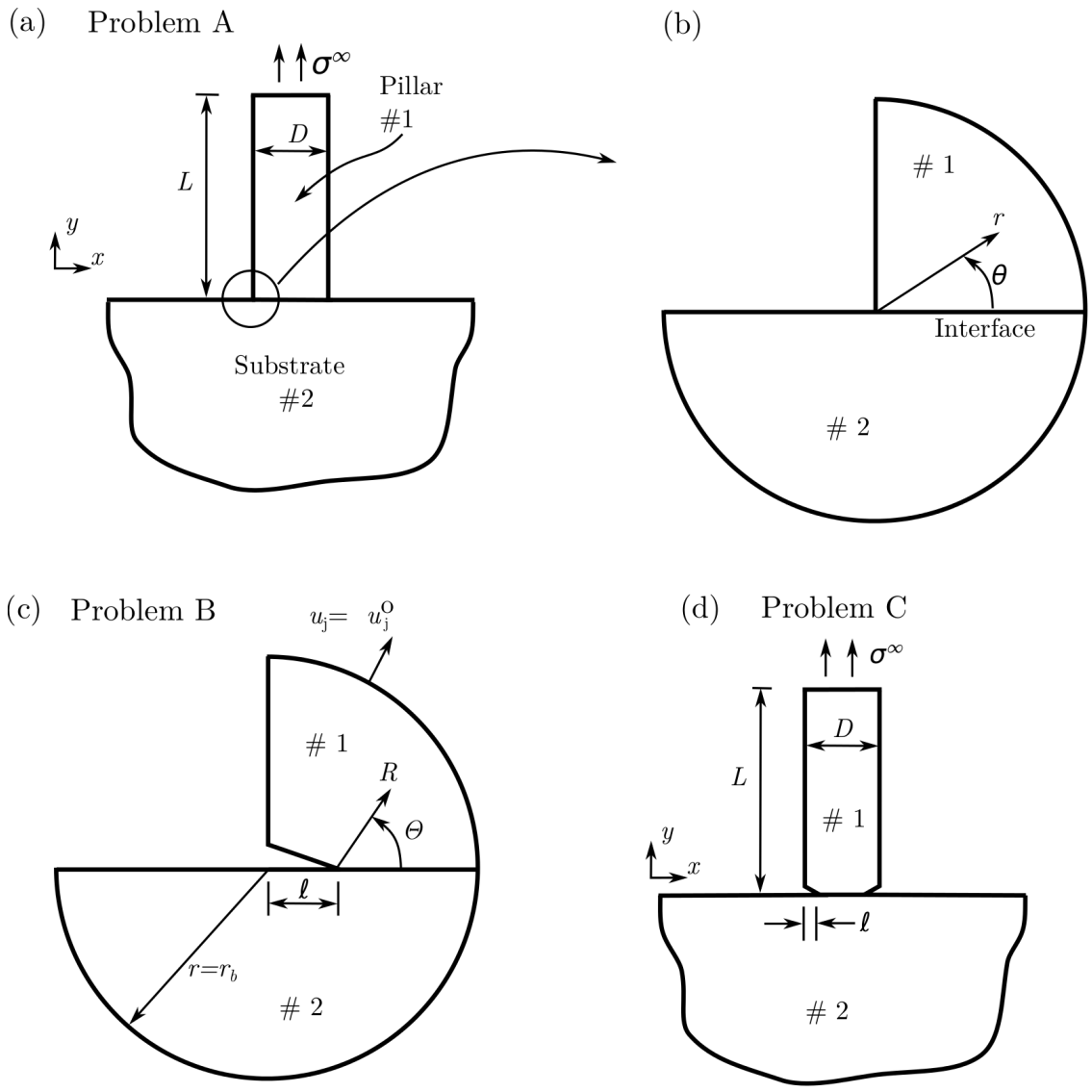

Figure 2: Schematic representation of the problems analysed. (a)-(b) Problem A: a pillar 1 is perfectly bonded to a substrate 2 and is subjected to a remote axial stress σ^∞. (c) Problem B: short crack ($\ell << D$) embedded within the domain of singularity. (d) Problem C: interfacial long crack of length ℓ.

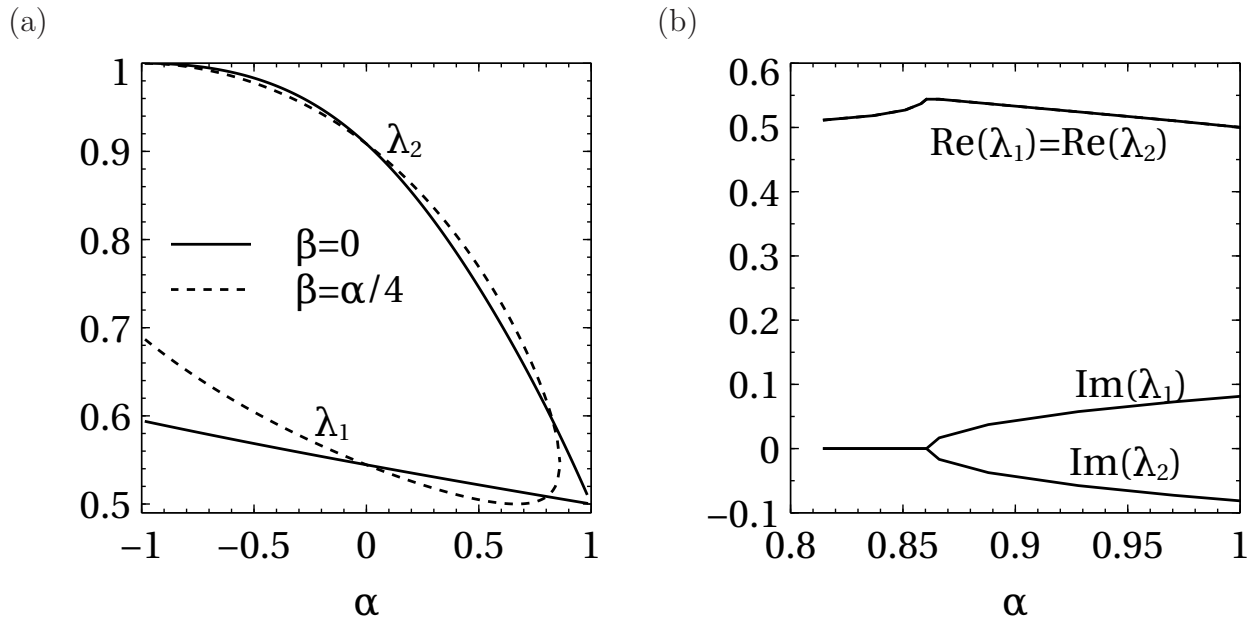

Figure 3: (a) Real eigenvalues (λ_1, λ_2) versus α for the corner singularity problem, for $\beta = 0$ and $\beta = \alpha/4$. (b) Complex eigenvalues, with real part $\mathrm{Re}(\lambda_n)$ and imaginary part $\mathrm{Im}\,(\lambda_n)$, for $0.86 < \alpha < 1$ and $\beta = \alpha/4$.

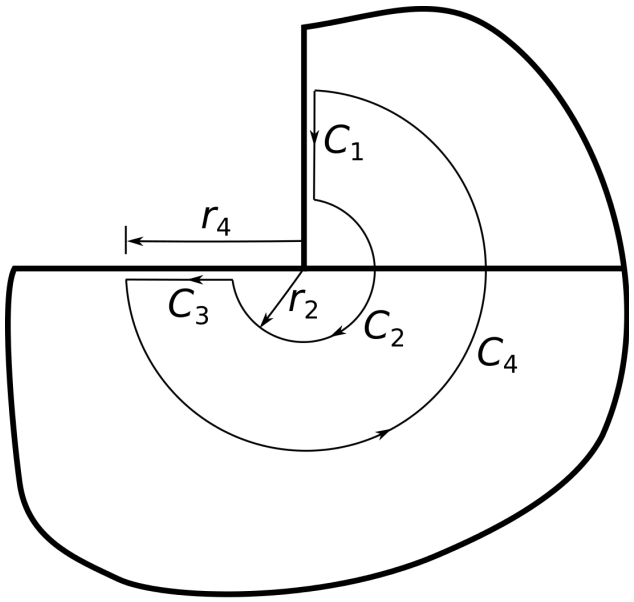

Figure 4: Contours used to evaluate the line integrals in (19).

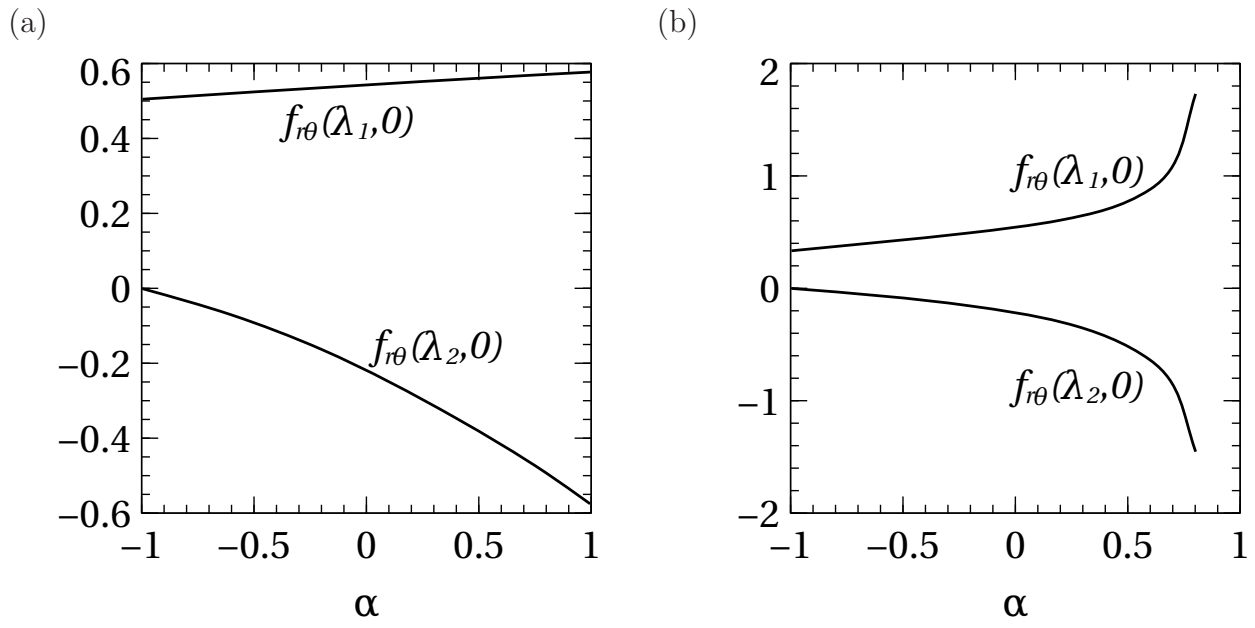

Figure 5: Value of $f_{r\theta}(\lambda_1, 0)$ and $f_{r\theta}(\lambda_2, 0)$ for eigenfields with intensities H_1 and H_2 a function of α for (a) $\beta = 0$ and (b) $\beta = \alpha/4$.

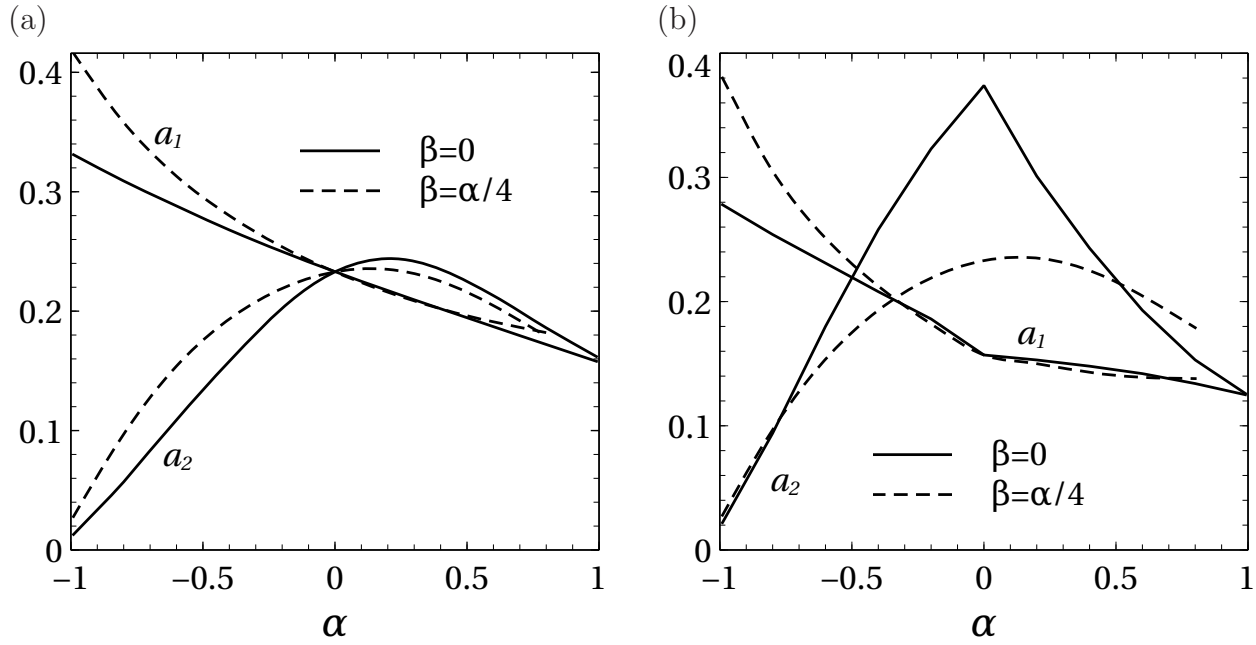

Figure 6: Calculated values of a_n versus α for (a) planar pillar and (b) cylindrical pillar.

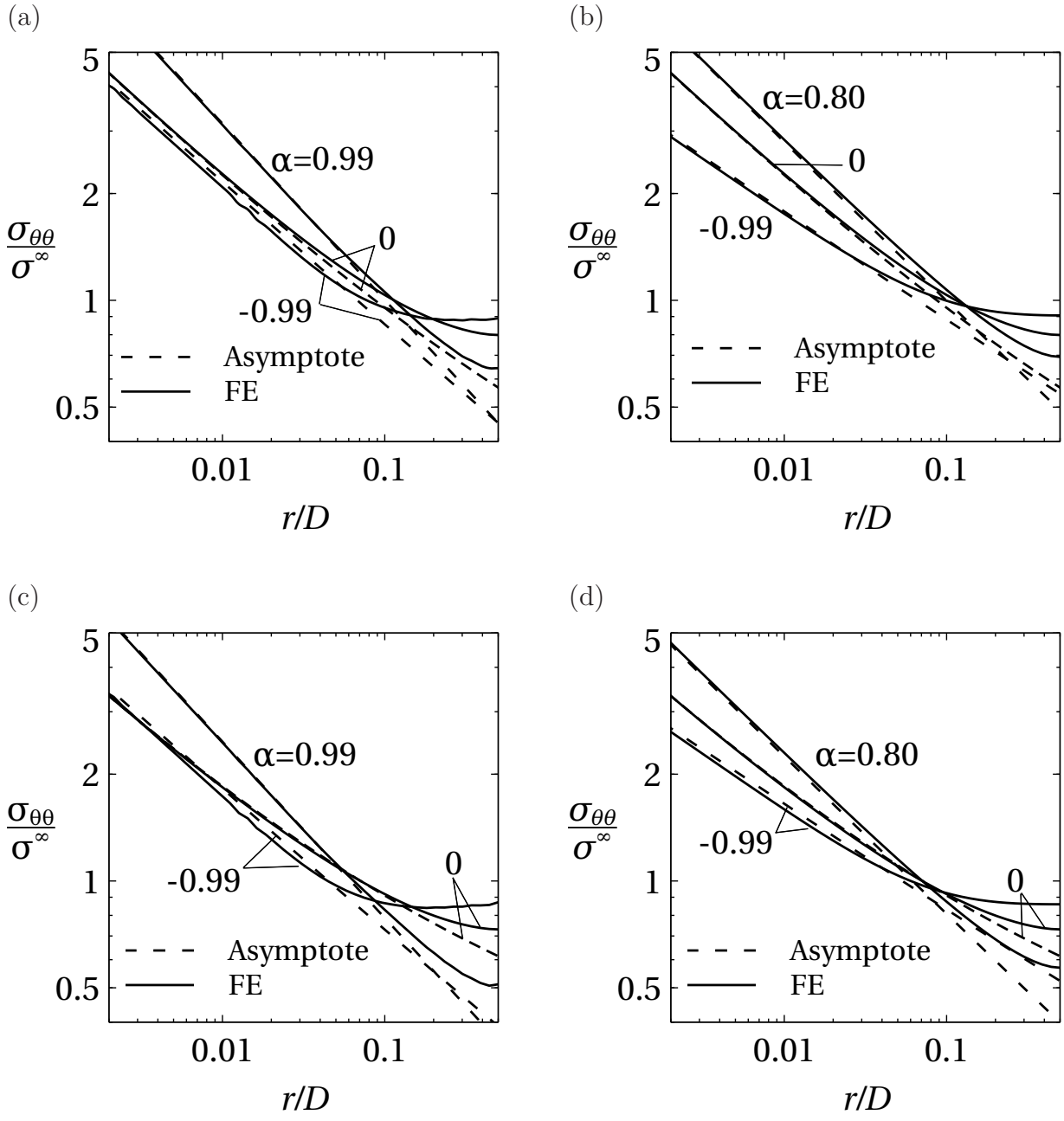

Figure 7: Normal traction ahead of corner for planar pillar with (a) $\beta = 0$, (b) $\beta = \alpha/4$, and for cylindrical pillar with (c) $\beta = 0$, (d) $\beta = \alpha/4$.

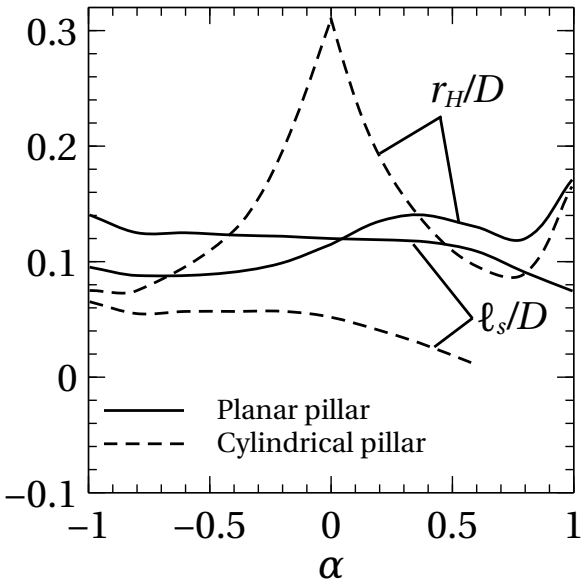

Figure 8: Domain of singularity r_H/D (based on traction) and ℓ_s (based on K) versus α, for $\beta = 0$.

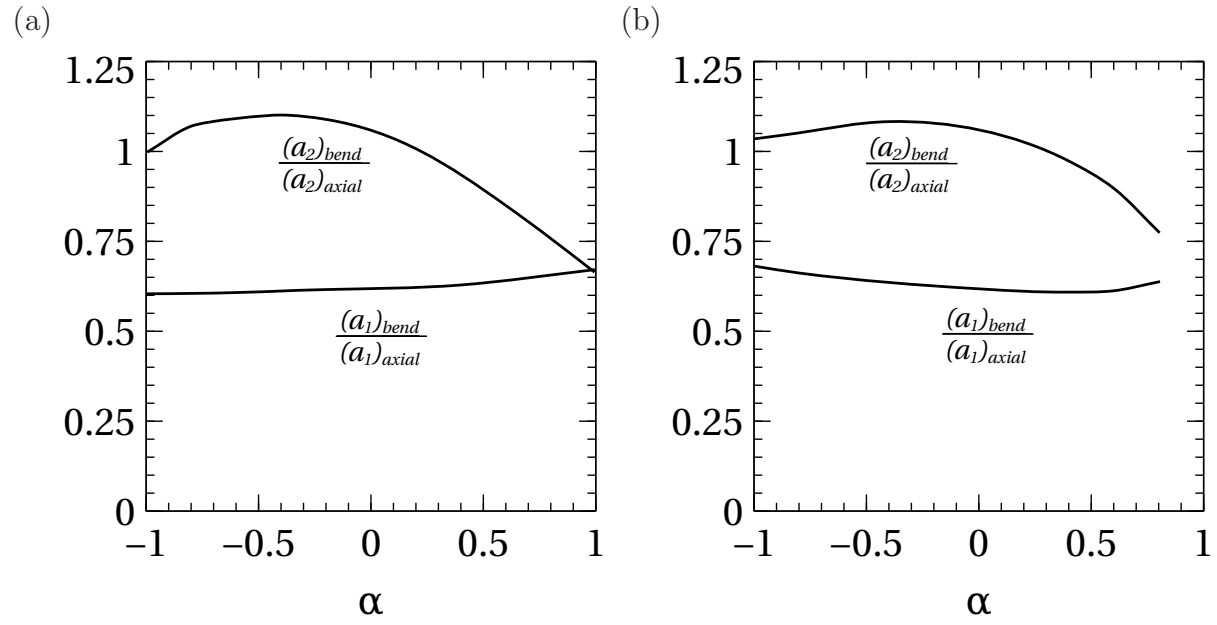

Figure 9: Ratio $(a_n)_{bend}/(a_n)_{axial}$ for a 2D planar pillar as a function of α for (a) $\beta = 0$ and (b) $\beta = \alpha/4$.

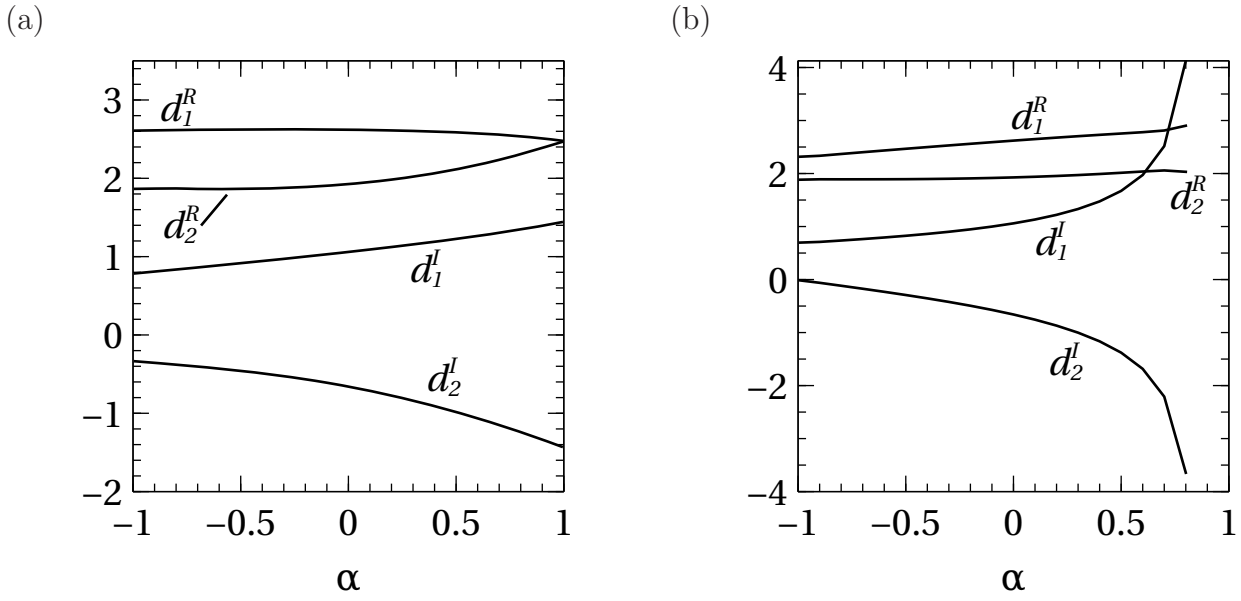

Figure 10: Calculated values of d_n^R and d_n^R versus α for (a) $\beta = 0$, (b) $\beta = \alpha/4$.

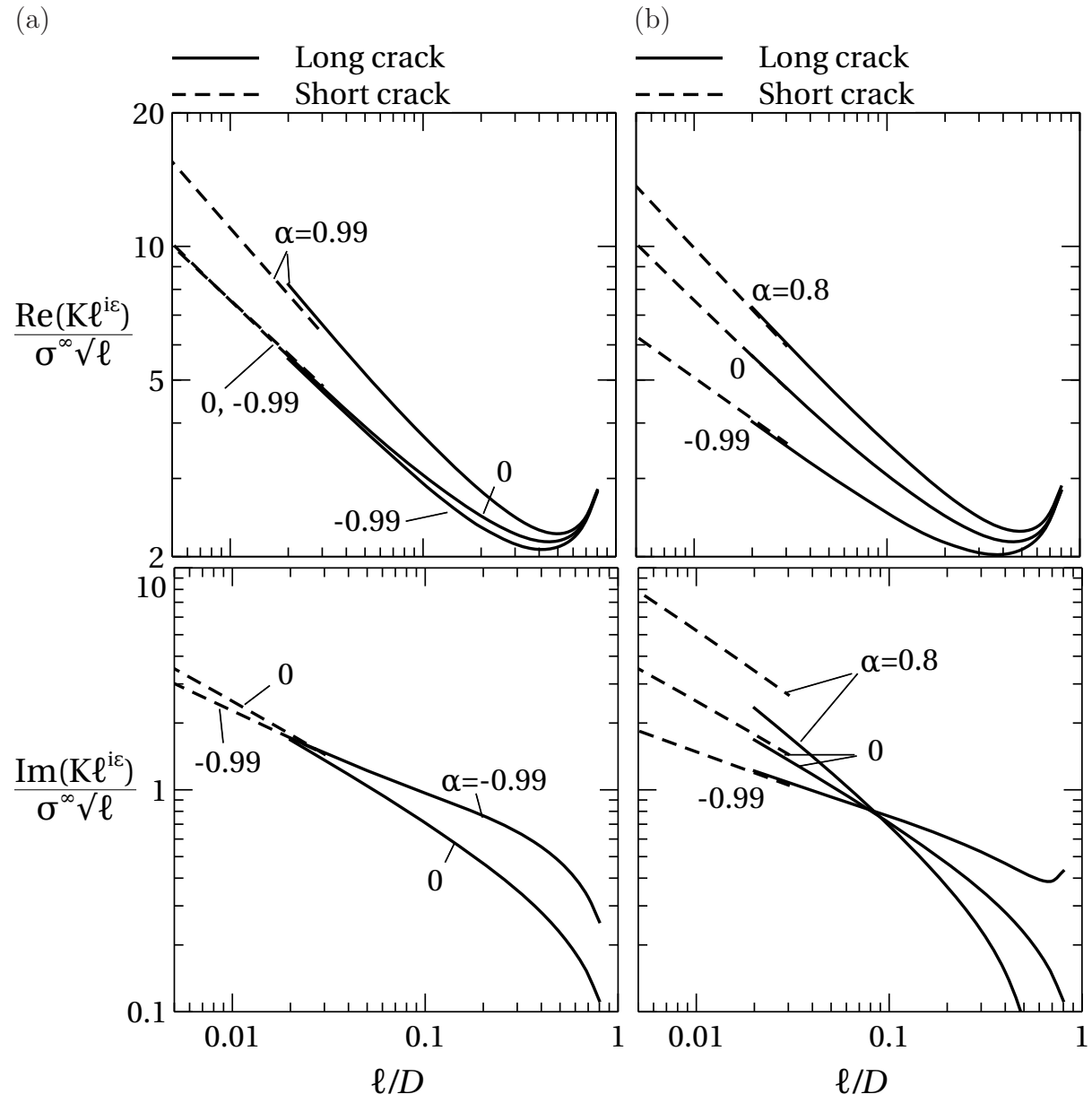

Figure 11: Real and imaginary parts of $K\ell^{i\epsilon}$ versus ℓ/D for planar pillar: (a) $\beta = 0$, (b) $\beta = \alpha/4$.

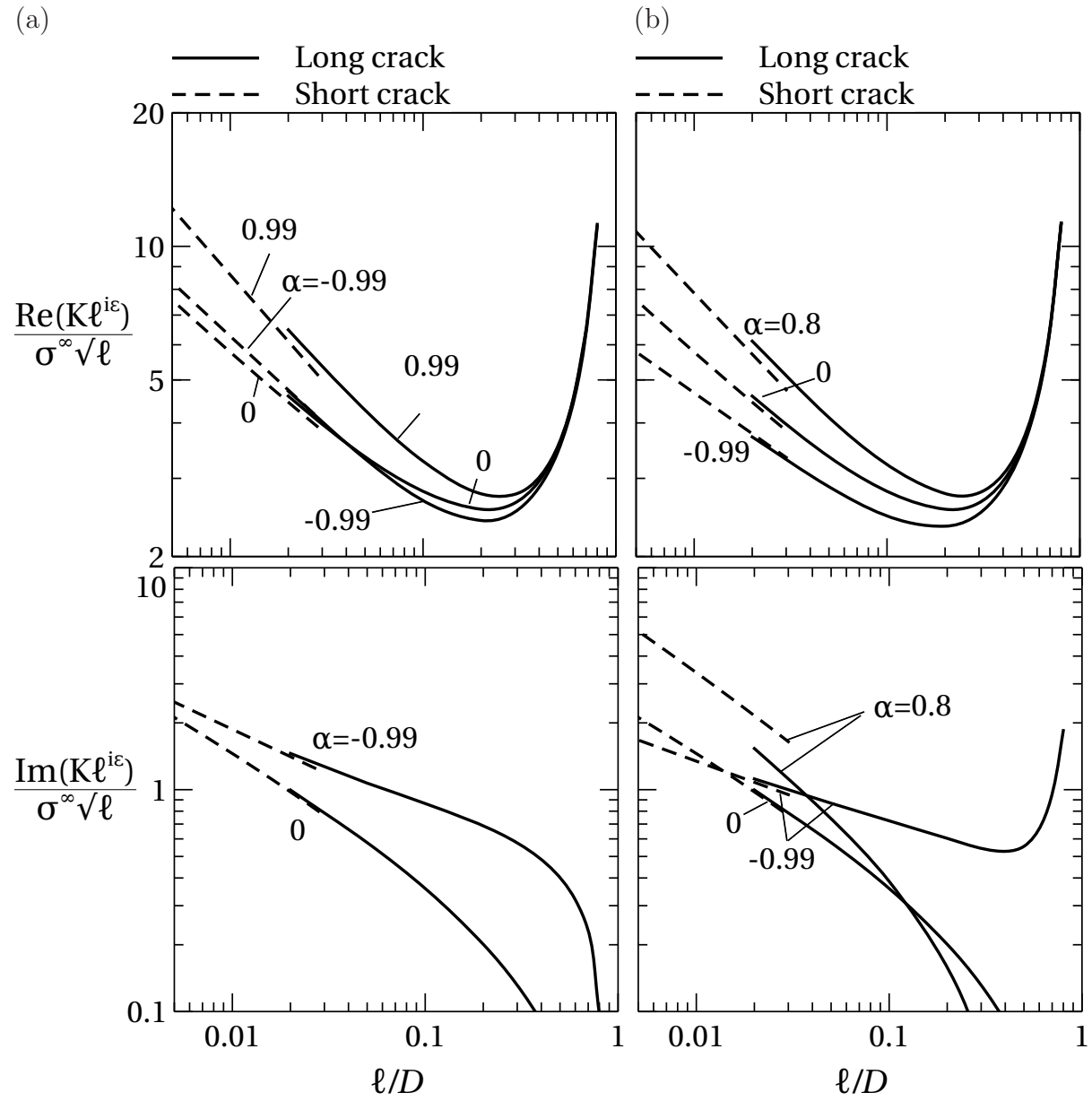

Figure 12: Real and imaginary parts of $K\ell^{i\epsilon}$ versus ℓ/D for cylindrical pillar: (a) $\beta = 0$, (b) $\beta = \alpha/4$.

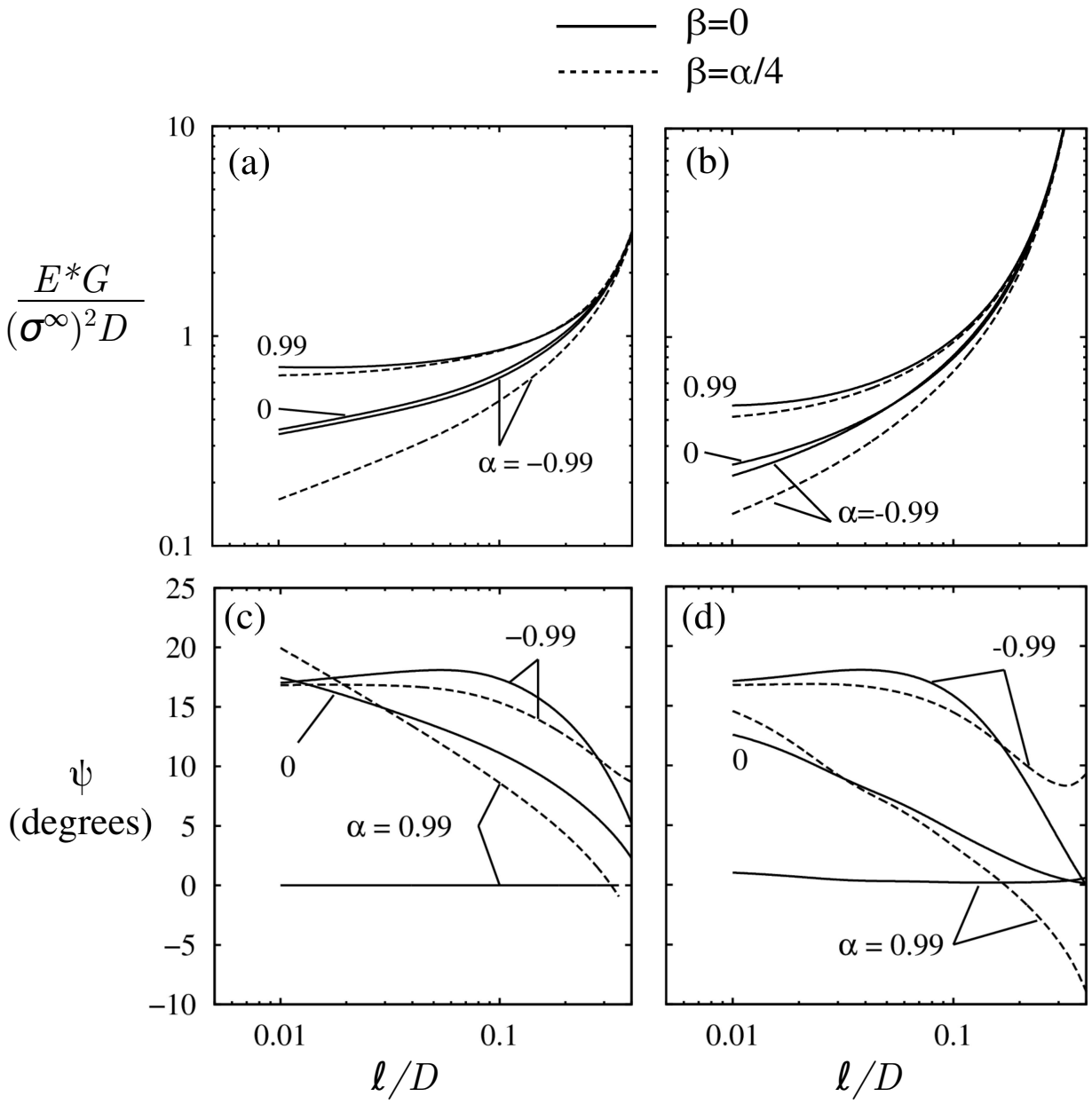

Figure 13: Energy release rate G versus ℓ/D for (a) planar and (b) cylindrical pillars. Phase angle ψ versus ℓ/D for (c) planar and (d) cylindrical pillars.

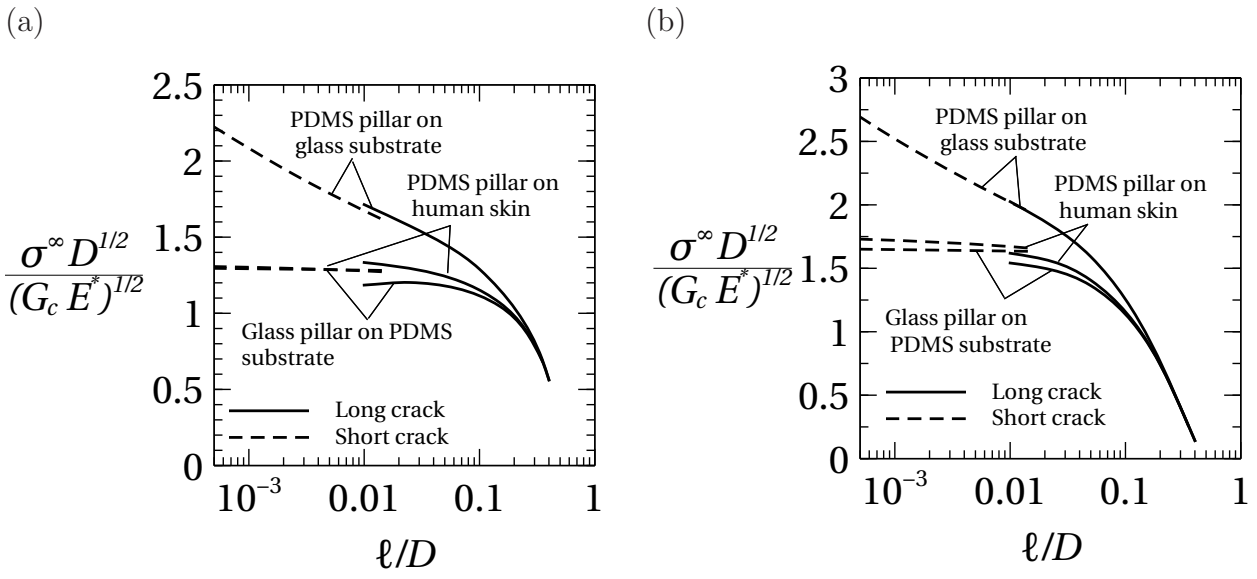

Figure 14: Normalised pull-off stress for a PDMS pillar from a glass substrate ($\alpha = -1, \beta = 0$), a glass pillar from a PDMS substrate ($\alpha = 1, \beta = 0$) and a PDMS pillar from human skin ($\alpha = 0.8, \beta = 0.2$): (a) planar pillar and (b) cylindrical pillar.

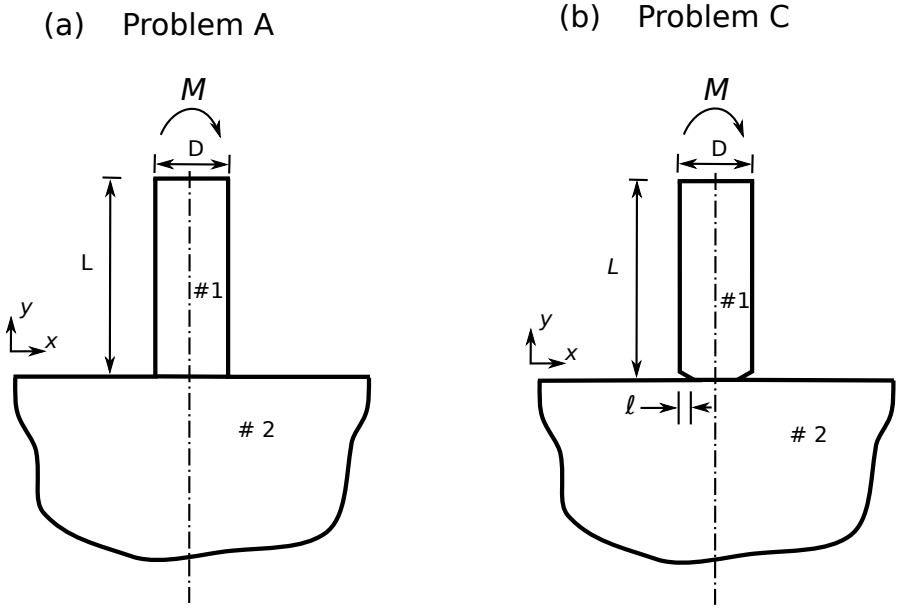

Figure 15: (a) Problem A: pillar perfectly bonded to the substrate with a remote moment M applied. (b) Problem C: interfacial long crack of length ℓ.

Table 1: Values of a_n and the $f_{r\theta}(\lambda_n, 0)$ for the corner singularity: planar pillar with a remote stress applied.

	$\beta = 0$				$\beta = \alpha/4$			
α	a_1	a_2	$f_{r\theta}(\lambda_1, 0)$	$f_{r\theta}(\lambda_2, 0)$	a_1	a_2	$f_{r\theta}(\lambda_1, 0)$	$f_{r\theta}(\lambda_2, 0)$
-0.99	0.331	0.013	0.505	-0.002	0.416	0.028	0.335	-0.002
-0.80	0.309	0.057	0.513	-0.034	0.358	0.097	0.373	-0.032
-0.60	0.288	0.109	0.521	-0.071	0.313	0.154	0.412	-0.067
-0.40	0.268	0.158	0.528	-0.114	0.280	0.193	0.452	-0.108
-0.20	0.250	0.202	0.536	-0.163	0.254	0.219	0.494	-0.157
0.00	0.233	0.233	0.543	-0.219	0.233	0.233	0.543	-0.219
0.20	0.217	0.244	0.550	-0.281	0.216	0.235	0.606	-0.302
0.40	0.202	0.235	0.557	-0.347	0.202	0.225	0.699	-0.423
0.60	0.187	0.213	0.564	-0.417	0.191	0.205	0.881	-0.639
0.80	0.172	0.186	0.571	-0.493	0.182	0.179	1.718	-1.442
0.99	0.158	0.162	0.577	-0.573	-	-	-	-

Table 2: Values of a_n for the corner singularity: cylindrical pillar with a remote stress applied.

	$\beta = 0$		$\beta = \alpha/4$	
α	a_1	a_2	a_1	a_2
-0.99	0.278	0.022	0.380	0.051
-0.80	0.254	0.094	0.305	0.174
-0.60	0.231	0.180	0.251	0.272
-0.40	0.208	0.258	0.212	0.330
-0.20	0.186	0.323	0.182	0.362
0.00	0.157	0.374	0.157	0.374
0.20	0.153	0.301	0.150	0.315
0.40	0.148	0.243	0.143	0.260
0.60	0.142	0.193	0.139	0.208
0.80	0.134	0.153	0.138	0.157
0.99	0.125	0.126	-	-

Table 3: Values of the calibration factor $b = b_R + ib_I$ for long cracks for $\beta = 0$, see (15).

		Plane strain		Axisymmetry				Plane strain		Axisymmetry	
α	ℓ/D	b_R	b_I	b_R	b_I	α	ℓ/D	b_R	b_I	b_R	b_I
-0.99	0.01	5.579	1.707	4.720	1.450	0.00	0.01	5.705	1.794	4.534	1.012
	0.05	2.923	0.965	2.674	0.863		0.05	3.055	0.708	2.802	0.360
	0.15	2.133	0.644	2.528	0.570		0.15	2.257	0.390	2.648	0.131
	0.25	2.102	0.473	3.445	0.387		0.25	2.172	0.255	3.516	0.064
	0.35	2.401	0.328	6.427	0.191		0.35	2.431	0.167	6.483	0.033
-0.80	0.01	5.562	1.758	4.677	1.455	0.20	0.01	5.855	1.706	4.736	1.010
	0.05	2.927	0.940	2.688	0.816		0.05	3.129	0.602	2.871	0.335
	0.15	2.153	0.603	2.548	0.513		0.15	2.291	0.324	2.670	0.114
	0.25	2.115	0.434	3.457	0.344		0.25	2.187	0.206	3.523	0.058
	0.35	2.407	0.297	6.438	0.173		0.35	2.437	0.133	6.480	0.044
-0.60	0.01	5.558	1.801	4.642	1.439	0.40	0.01	6.097	1.536	4.989	0.957
	0.05	2.940	0.904	2.709	0.756		0.05	3.227	0.467	2.950	0.294
	0.15	2.175	0.557	2.569	0.449		0.15	2.327	0.252	2.692	0.094
	0.25	2.128	0.391	3.470	0.296		0.25	2.203	0.156	3.530	0.051
	0.35	2.413	0.265	6.448	0.153		0.35	2.443	0.099	6.476	0.055
-0.40	0.01	5.573	1.828	4.618	1.390	0.60	0.01	6.482	1.244	5.320	0.820
	0.05	2.964	0.855	2.736	0.676		0.05	3.358	0.294	3.042	0.232
	0.15	2.200	0.506	2.592	0.376		0.15	2.368	0.172	2.715	0.072
	0.25	2.142	0.347	3.484	0.243		0.25	2.220	0.103	3.537	0.044
	0.35	2.419	0.233	6.459	0.130		0.35	2.449	0.065	6.473	0.067
-0.20	0.01	5.618	1.829	4.601	1.281	0.80	0.01	7.089	0.757	5.777	0.533
	0.05	3.002	0.791	2.770	0.563		0.05	3.532	0.074	3.150	0.136
	0.15	2.227	0.451	2.618	0.284		0.15	2.412	0.085	2.738	0.039
	0.25	2.157	0.302	3.498	0.177		0.25	2.238	0.049	3.540	0.025
	0.35	2.425	0.200	6.470	0.098		0.35	2.455	0.030	6.456	0.042

Table 4: Values of the calibration factor $b = b_R + ib_I$ for long cracks for $\beta = \alpha/4$.

		Plane strain		Axisymmetry				Plane strain		Axisymmetry	
α	ℓ/D	b_R	b_I	b_R	b_I	α	ℓ/D	b_R	b_I	b_R	b_I
-0.99	0.01	4.027	1.217	3.718	1.118	0.00	0.01	5.705	1.794	4.534	1.012
	0.05	2.510	0.757	2.468	0.723		0.05	3.055	0.708	2.802	0.360
	0.15	2.038	0.525	2.501	0.546		0.15	2.257	0.390	2.648	0.131
	0.25	2.075	0.422	3.464	0.555		0.25	2.172	0.255	3.516	0.064
	0.35	2.408	0.388	6.511	0.964		0.35	2.431	0.167	6.483	0.033
-0.80	0.01	4.343	1.307	3.869	1.120	0.20	0.01	6.063	1.962	4.856	1.121
	0.05	2.611	0.746	2.526	0.671		0.05	3.178	0.702	2.900	0.360
	0.15	2.079	0.497	2.526	0.477		0.15	2.305	0.368	2.679	0.105
	0.25	2.091	0.387	3.468	0.467		0.25	2.197	0.225	3.530	0.012
	0.35	2.406	0.342	6.492	0.785		0.35	2.445	0.125	6.489	-0.118
-0.60	0.01	4.678	1.409	4.033	1.120	0.40	0.01	6.436	2.159	5.193	1.247
	0.05	2.718	0.735	2.590	0.614		0.05	3.309	0.697	3.002	0.364
	0.15	2.123	0.469	2.553	0.404		0.15	2.355	0.347	2.713	0.083
	0.25	2.108	0.352	3.475	0.375		0.25	2.224	0.197	3.548	-0.037
	0.35	2.408	0.296	6.479	0.601		0.35	2.463	0.085	6.503	-0.269
-0.40	0.01	5.015	1.522	4.202	1.114	0.60	0.01	6.831	2.391	5.550	1.394
	0.05	2.826	0.725	2.657	0.551		0.05	3.452	0.693	3.109	0.375
	0.15	2.167	0.441	2.582	0.327		0.15	2.407	0.330	2.749	0.067
	0.25	2.128	0.318	3.486	0.282		0.25	2.254	0.171	3.572	-0.084
	0.35	2.412	0.252	6.474	0.418		0.35	2.484	0.044	6.527	-0.420
-0.20	0.01	5.357	1.649	4.374	1.089	0.80	0.01	7.264	2.665	5.940	1.560
	0.05	2.938	0.716	2.728	0.473		0.05	3.366	0.731	3.220	0.396
	0.15	2.211	0.415	2.614	0.242		0.15	2.463	0.315	2.790	0.057
	0.25	2.149	0.286	3.499	0.183		0.25	2.288	0.146	3.602	-0.128
	0.35	2.420	0.209	6.475	0.232		0.35	2.510	0.004	6.561	-0.574

Table 5: Summary of results for compliance $\mathcal{C} = f_1(\nu_2)(1-\nu_2^2)/DE_2$, energy release rate $G = f_2(\nu_2)(1-\nu_2^2)D(\sigma^\infty)^2/E_2$ and phase angle $\hat{\psi}$ for 2D planar and 3D cylindrical pillars for $\alpha = 1$ and arbitrary β.

Punch	$f_1(\nu_2)$	$f_2(\nu_2)$	$\hat{\psi}(\hat{\ell} = D)$
2D frictionless	∞	$1/\pi$	Mode I
2D sticking	∞	$1/\pi$	0
3D frictionless	1	$\pi/16$	Mode I
3D sticking	$\frac{1-2\nu_2}{(1-\nu_2)\ln(3-4\nu_2)}$	$\frac{\pi}{16}\frac{(1-2\nu_2)}{(1-\nu_2)\ln(3-4\nu_2)}$	$-\frac{\ln 4}{2\pi}\ln(3-4\nu_2)$

Table 6: Values of the calibration factor for the corner singularity, see (5): planar pillar with a remote moment applied.

	$\beta = 0$		$\beta = \alpha/4$	
α	a_1	a_2	a_1	a_2
-0.99	0.197	0.013	0.283	0.029
-0.80	0.187	0.061	0.237	0.102
-0.60	0.175	0.119	0.203	0.165
-0.40	0.164	0.174	0.178	0.209
-0.20	0.153	0.220	0.159	0.236
-0.00	0.144	0.247	0.144	0.247
0.20	0.135	0.246	0.132	0.241
0.40	0.127	0.220	0.123	0.219
0.60	0.120	0.181	0.117	0.184
0.80	0.113	0.141	0.116	0.139
0.99	0.106	0.108	-	-

Table 7: Values of the calibration factor $b = b_R + ib_I$ for long cracks when an end moment is applied to a planar punch.

		$\beta = 0$		$\beta = \alpha/4$				$\beta = 0$		$\beta = \alpha/4$	
α	l/D	b_R	b_I	b_R	b_I	α	l/D	b_R	b_I	b_R	b_I
-0.99	0.01	3.450	1.076	2.841	0.838	0.00	0.01	3.912	0.998	3.912	0.998
	0.05	2.148	0.570	2.053	0.493		0.05	2.398	0.367	2.398	0.367
	0.15	2.181	0.255	2.181	0.345		0.15	2.259	0.134	2.259	0.134
	0.25	2.971	0.120	2.976	0.434		0.25	2.983	0.060	2.983	0.060
	0.35	5.417	0.046	5.470	0.998		0.35	5.464	0.023	5.464	0.023
-0.80	0.01	3.501	1.088	3.039	0.867	0.20	0.01	4.090	0.914	4.157	1.035
	0.05	2.187	0.539	2.117	0.471		0.05	2.462	0.310	2.474	0.338
	0.15	2.196	0.232	2.192	0.304		0.15	2.275	0.108	2.280	0.091
	0.25	2.966	0.108	2.974	0.360		0.25	2.988	0.048	2.991	-0.013
	0.35	5.458	0.041	5.465	0.804		0.35	5.465	0.018	5.467	-0.169
-0.60	0.01	3.571	1.091	3.248	0.898	0.40	0.01	4.317	0.789	4.422	1.073
	0.05	2.234	0.503	2.185	0.446		0.05	2.532	0.245	2.553	0.309
	0.15	2.211	0.208	2.207	0.261		0.15	2.292	0.082	2.303	0.048
	0.25	2.969	0.096	2.972	0.284		0.25	2.993	0.036	3.002	-0.088
	0.35	5.460	0.037	5.462	0.604		0.35	5.466	0.013	5.471	-0.362
-0.40	0.01	3.659	1.079	3.462	0.930	0.60	0.01	4.609	0.610	4.718	1.112
	0.05	2.284	0.463	2.255	0.421		0.05	2.609	0.173	2.639	0.277
	0.15	2.227	0.184	2.224	0.219		0.15	2.309	0.055	2.328	0.004
	0.25	2.974	0.084	2.975	0.209		0.25	2.998	0.024	3.015	-0.164
	0.35	5.461	0.032	5.464	0.408		0.35	5.467	0.009	5.476	-0.558
-0.20	0.01	3.771	1.050	3.684	0.963	0.80	0.01	4.986	0.356	5.057	1.148
	0.05	2.338	0.418	2.325	0.395		0.05	2.693	0.091	2.731	0.244
	0.15	2.243	0.159	2.241	0.177		0.15	2.326	0.027	2.356	-0.040
	0.25	2.978	0.072	2.978	0.134		0.25	3.003	0.012	3.030	-0.241
	0.35	5.463	0.027	5.465	0.215		0.35	5.468	0.004	5.483	-0.758